Large-eddy simulation of flow over a grooved cylinder up to transcritical Reynolds numbers

W. Cheng[1,2,†], D. I. Pullin[2] and R. Samtaney[1]

[1]Mechanical Engineering, Physical Science and Engineering Division, King Abdullah University of Science and Technology, Thuwal, 23955-6900, Saudi Arabia

[2]Graduate Aerospace Laboratories, California Institute of Technology, CA 91125, USA

We report wall-resolved large-eddy simulation (LES) of flow over a grooved cylinder up to the transcritical regime. The stretched-vortex subgrid-scale model is embedded in a general fourth-order finite-difference code discretization on a curvilinear mesh. In the present study 32 grooves are equally distributed around the circumference of the cylinder, each of sinusoidal shape with height ϵ, invariant in the spanwise direction. Based on the two parameters, ϵ/D and the Reynolds number $Re_D = U_\infty D/\nu$ where U_∞ is the free-stream velocity, D the diameter of the cylinder and ν the kinematic viscosity, two main sets of simulations are described. The first set varies ϵ/D from 0 to 1/32 while fixing $Re_D = 3.9 \times 10^3$. We study the flow deviation from the smooth-cylinder case, with emphasis on several important statistics such as the length of the mean-flow recirculation bubble L_B, the pressure coefficient C_p, the skin-friction coefficient $C_{f\theta}$ and the non-dimensional pressure gradient parameter β. It is found that, with increasing ϵ/D at fixed Re_D, some properties of the mean flow behave somewhat similarly to changes in the smooth-cylinder flow when Re_D is increased. This includes shrinking L_B and nearly constant minimum pressure coefficient. In contrast, while the non-dimensional pressure gradient parameter β remains nearly constant for the front part of the smooth cylinder flow, β shows an oscillatory variation for the grooved-cylinder case. The second main set of LES varies Re_D from 3.9×10^3 to 6×10^4 with fixed $\epsilon/D = 1/32$. It is found that this Re_D range spans the subcritical and supercritical regimes and reaches the beginning of the transcritical flow regime. Mean-flow properties are diagnosed and compared with available experimental data including C_p and the drag coefficient C_D. The timewise variation of the lift and drag coefficients are also studied to elucidate the transition among three regimes. Instantaneous images of the surface, skin-friction vector field and also of the three-dimensional Q-criterion field are utilized to further understand the dynamics of the near-surface flow structures and vortex shedding. Comparison of the grooved-cylinder flow with the equivalent flow over a smooth-wall cylinder shows structural similarities but significant differences. Both flows exhibit a clear common signature, which is the formation of mean-flow secondary separation bubbles that transform to other local flow features upstream of the main separation region (prior separation bubbles) as Re_D is increased through the respective drag crises. Based on these similarities it is hypothesized that the drag crises known to occur for flow past a cylinder with different surface topographies is the result of a change in the global flow state generated by an interaction of primary flow separation with secondary

† Email address for correspondence: chengw@caltech.edu

flow recirculating motions that manifest as a mean-flow secondary bubble. For the smooth-wall flow this is accompanied by local boundary-layer flow transition to turbulence and a strong drag crisis, while for the grooved-cylinder case the flow remains laminar but unsteady through its drag crisis and into the early transcritical flow range.

Key words: boundary layer separation, turbulence simulation, turbulent flows

1. Introduction

The flow over a bluff body, especially a canonical geometry such as a circular cylinder, has attracted much attention within the fluid mechanics community in the past hundred years. For a smooth-walled cylinder, the behaviour of the mean-flow separation bubble can be identified with three distinct regimes. With increasing Reynolds numbers, these are the subcritical, the supercritical and the transcritical flow regimes. If we define $Re_D = U_\infty D/\nu$ for a Newtonian fluid where U_∞ is the free-stream velocity, D is the diameter of the cylinder and ν is the kinematic viscosity of the fluid, the transition from the subcritical to the supercritical regime is in the band $Re_D \in (2.6 \times 10^5, 3.5 \times 10^5)$. A well-known phenomenon observed in this transition is the drag crisis, where the drag coefficient C_D decreases sharply. A generally accepted explanation of this transition is related to the location of turbulent transition, which is inside the wake flow for the subcritical regime, moving upstream of primary separation as Re_D increases while residing on a prior mean-flow separation bubble for the supercritical regime. Here 'prior' is taken to define the bubble's location, upstream of the mean-flow, primary recirculation bubble. Recently, Cheng *et al.* (2017) have observed that the secondary separation bubble, which lies inside the primary recirculation bubble in the subcritical regime, is the mean-flow manifestation of strongly unsteady and three-dimensional reattachment cells in this regime. As Re_D increases, the subcritical to supercritical transition is a result of near-surface transition to turbulence stimulated by the dynamical interaction of these reattachment cells with the separation shear layer of the primary separation bubble.

Another interesting transition is from the supercritical to transcritical regime. According to Roshko (1961), this transition range should be characterized by the disappearance of the prior separation bubble together with the abatement of coherent vortex shedding at its lower bound, at approximately $Re_D = 0.9 \times 10^6$, followed by recurrence of vortex shedding at the transition upper bound at around $Re_D = 3.5 \times 10^6$. Nonetheless, a clear picture of its transition remains elusive, perhaps because several successive phases of instability occur over a relatively narrow range of Re_D, making experimental investigation difficult (Schewe 1983).

In order to clarify the dominant flow physics active within the subcritical, supercritical and transcritical regimes and their respective transitions, a natural variation is to consider the non-smooth cylinder where geometric surface perturbations are prescribed. The experimental study of cylinder flow with a non-smooth surface has been conducted in parallel to the smooth-cylinder counterpart. Generally, it is expected that the Reynolds number range characterizing regime transitions for non-smooth surface cylinder flow should be rather different to the smooth-cylinder case, since the non-smooth surface may trap small-scale recirculating flow regions associated with the near-wall flow. This may even result in overlapping of the two transitions.

Earlier experimental studies of flow over cylinder with three-dimensional roughness or surface perturbations have clearly shown that increasing a roughness size parameter leads to decreasing critical Reynolds numbers. Here 'critical' means the transition from the subcritical to the supercritical regime as diagnosed by a sudden decrease in C_D. For example, Fage & Warsap (1929) demonstrated that the transitions among three regimes can take place at lower Reynolds number for strongly rough-walled cylinders, even reaching the transcritical regime at $Re_D = 5 \times 10^4$. It is also clearly shown by Fage & Warsap (1929) that in the transcritical regime, a large roughness scale corresponds to a high drag coefficient. Achenbach (1971) reported skin-friction and wall pressure-coefficient distributions for different cylinder surface roughness levels. From his skin-friction results, near-wall laminar flow, flow with laminar–turbulent transition in the front part of the cylinder and even almost fully turbulent flow, are clearly captured. The skin-friction distribution at $Re_D = 3 \times 10^6$ at medium roughness shows fully turbulent behaviour around the cylinder. This flow character has not been reported in smooth-wall cylinder experiments, since it is expected to take place at approximately $Re_D \approx 10^8$, which is largely beyond the present capability of wind/water tunnel testing.

For a cylinder with a 'small' roughness scale where 'small' here is taken to mean critical Reynolds number larger than 10^5, Szechenyi (1975) found that the product of the critical Reynolds number and the roughness height provides a common value of 200 for all small roughness cases. They claimed similarities between flow over a small roughness cylinder and a smooth cylinder. This is not characteristic of flow past cylinders with strong surface-geometry perturbations. Güven, Farell & Patel (1980) performed rough-cylinder flow experiments, reporting detailed surface pressure-coefficient distributions. Their results agree reasonably with Achenbach (1971) although different kinds of roughness elements were employed. For cases in the transcritical regime, their data show large surface roughness resulting in a smaller pressure 'rise', with 'rise' defined from the difference value between the minimal and the plateau values. This effect results in a higher drag coefficient. An explanation provided by Güven *et al.* (1980) is that large surface roughness leads to a thicker boundary layer with larger momentum deficit which separates earlier than for flows with smaller surface roughness. Another experiment by Achenbach & Heinecke (1981) focused on the non-steady wake flow for a cylinder with a rough surface. For relatively large roughness elements, regular vortex shedding is found for all Re_D, which seems to avoid the successive instability phenomena due to turbulent transition as suggested by Schewe (1983). A notable result for vortex shedding is that shedding frequencies in the transcritical regime are quite similar for many different surfaces, with deviations of only 7 % from the mean value for all roughness parameters tested.

It is recognized that the term 'rough wall' may have a broad range of geometrical and fluid-dynamical interpretations. For a turbulent boundary-layer flow over surfaces that can be quantified by an equivalent sand grain roughness, one conventional concept of rough-wall flow requires that the roughness height should be sufficiently small compared to the local wall layer thickness so as to allow the existence of at least a partial log-law region. Hence the roughness height should be around or less than a few per cent of the boundary-layer thickness (Jiménez 2004). In contrast, for the flow geometry considered by Achenbach & Heinecke (1981), the 'roughness' consisted of a regular three-dimensional pyramid (R3DP) perturbation of the cylinder surface with 36 wavelengths around the circumference, and with a perturbation amplitude that cannot satisfy the traditional idea of roughness. Nonetheless, their experiments indicate that an R3DP cylinder flow can exhibit qualitatively similar Reynolds-number-dependent

Source	Perturbation type	Present description
Yamagishi & Oki (2004)	2-D arc/triangle groove	Arc groove, triangle groove
Achenbach & Heinecke (1981)	Pyramid	Regular 3-D pyramid (R3DP)
Güven *et al.* (1980)	Sand-grain commercial paper	Sand perturbation
Achenbach (1971)	Emery paper	Emery perturbation
Fage & Warsap (1929)	Glass paper	Glass perturbation

TABLE 1. Summary of experimental data cited in the present study.

flow characteristics to those of a small-scale, surface roughness flow. This could suggest that, for example, the drag crisis is not a phenomenon associated with the presence of a canonical turbulent boundary layer.

Another interesting geometry for the study of bluff-body flow regimes at reduced Re_D (compared to the smooth-wall case) is the cylinder with two-dimensional (2-D) or groove-shaped geometric perturbations. Here the geometry consists of a pattern in the circumferential direction only, with cylindrical invariance in the spanwise or axial direction. Yamagishi & Oki (2004) investigated experimentally flow over a grooved cylinder for $Re_D \in (10^4$ to $10^5)$. Use of both triangular and arc-shaped grooves in their experiments were found to cover all of the subcritical, supercritical and transcritical flow regimes. A summary of the cylinder surface perturbations for the experiments discussed above is provided in table 1.

Direct numerical simulation (DNS), which is accurate and resolves both the Kolmogorov scale and the viscous wall unit, presently appears limited to cylinder flow up to $Re_D = O(10^4)$, which is far from the interesting transition between regimes for the smooth-wall cylinder. Wall-resolved large-eddy simulation (LES), in which large scales are resolved and small scales are modelled via a subgrid-scale (SGS) model, has been successful for high-fidelity flow simulation up to substantially higher Re_D when compared to DNS. Both Lehmkuhl *et al.* (2014) and Cheng *et al.* (2017) implemented LES of flow over smooth cylinder up to $Re_D \approx 8 \times 10^5$. These simulations reach the supercritical regime but do not penetrate the transcritical regime.

For a non-smooth cylinder, it is expected that wall-resolved LES will have more stringent resolution requirements than the smooth-wall cylinder at the same Re_D. Typically, in LES of flow past a two-dimensional body, such as either the smooth or grooved cylinder, the mesh size in the spanwise direction usually can be chosen to be up to 10 or more times the wall-normal mesh size (Choi & Moin 2012). Thus wall-resolved LES of cylinder with truly three-dimensional geometric perturbation would require a fine mesh in the spanwise direction while the grooved cylinder can employ a relatively coarser spanwise mesh thus maximizing the effectiveness of LES for this type of flow. Hence, presently we focus on the flow over grooved cylinders and investigate the flow behaviour in the subcritical, supercritical and lower transcritical regimes. We will emphasize the comparison of grooved-wall cylinder flow with similar phenomena in flow over the smooth cylinder, with the aim of providing a more robust understanding of the canonical flow over a cylinder.

In what follows, the LES framework and cases implemented will be outlined in § 2. In § 3 we consider the results from the first set of LES at $Re_D = 3.9 \times 10^3$ and study the effect of different groove amplitude or height. Then with a fixed groove geometry, we discuss the effect of varying Re_D and explore the different flow regimes in § 4. Additionally, in § 5 we focus on the instantaneous flow field, and analyse the flow properties and structures revealed within the groove cavities themselves and structures

seen during unsteady vortex shedding. Following some discussion of the drag crisis and regime transition in § 6, concluding remarks and a new hypothesis concerning the base dynamical mechanism of the drag crisis for general cylinder flows are provided in § 7.

2. Numerical method, physical model and cases set-up

2.1. *Numerical method and physical model*

The fractional-step method by Zang, Street & Koseff (1994) is applied to solve the three-dimensional, incompressible, LES versions of the Navier–Stokes equations on a curvilinear mesh, combined with the third-order Runge–Kutta method by Spalart, Moser & Rogers (1991) for time stepping. Periodic boundary conditions in the spanwise or y direction are used. For spatial discretization, fourth-order finite-difference schemes, which are essentially dispersive rather than dissipative, are utilized for all three directions.

Although the LES described presently were performed using curvilinear coordinates (ξ, y, η) that body-fit the grooved-cylinder, two-dimensional geometry, results will be discussed using both cylindrical coordinates (θ, y, r) with $-\pi < \theta \leqslant \pi$, velocity components (u_θ, u_y, u_r) and Cartesian coordinates (x, y, z) with corresponding velocity components (u_x, u_y, u_z). In generating meshes, first, O-type grids were initialized in the computational domain, with uniform grid point distribution along the circumferential direction and with stretching used in the radial direction. Then, in the near-wall region, the grid is further refined in order to ensure orthogonality of the near-wall mesh.

In simulation, the free-stream flow is in the positive x direction. At the wall the no-slip condition is implemented at the order of accuracy of the overall numerical method. For the outer boundary, Dirichlet boundary conditions are applied on the windward part with $u_x = U_\infty$ and $u_y = 0$, $u_z = 0$. On the leeward outer boundary, convective boundary conditions are used. Periodic boundary conditions are used in the spanwise direction. To damp down numerical oscillation induced by the outer flow at the curved boundary, a viscous sponge layer is applied for $0.8L_r \leqslant r \leqslant L_r$ with L_r the external domain in the r direction, similar to the viscous sponge techniques used in numerical simulation of flow over bluff objects by Karniadakis & Triantafyllou (1992) and Mittal & Balachandar (1996). In the present study, $L_r = 50$ is employed for all cases. In the spanwise direction, a domain size $L_y = 3D$ is used for all cases. Generally $3D$ is considered sufficient for smooth-surface cylinders with $Re_D \geqslant 3.9 \times 10^3$ (Beaudan & Moin 1994). It should also be sufficient for the present study where the presence of geometrical surface perturbations in the circumferential direction which will tend to break up large-scale structures.

2.2. *Physical model*

In closing the LES framework, the stretched-vortex (SV) subgrid-scale (SGS) model (Misra & Pullin 1997; Chung & Pullin 2009) is adopted. The basic version of the present code has been implemented in many cases with careful verification, which include DNS of airfoil flow (Zhang *et al.* 2015) and LES of smooth-walled cylinder flow (Cheng *et al.* 2017).

The SV model utilizes a structure-based representation of small-scale, unresolved fluid motion modelled by virtual SGS vortices that are stretched by the strain rate field provided by the local resolved-scale flow. Specifically in each computational cell the

subgrid motion is dominated by a SGS vortex with direction vector $\boldsymbol{e}^v$. The subgrid stress can thus be described as (Misra & Pullin 1997)

$$T_{ij} = (\delta_{ij} - \boldsymbol{e}_i^v \boldsymbol{e}_j^v)K, \tag{2.1}$$

with K the subgrid kinetic energy. This kinetic energy, which is defined as an integral of the SGS energy spectrum, can be computed as (see Voelkl, Pullin & Chan (2000) for details)

$$K = \int_{k_c}^{\infty} E(k)\, \mathrm{d}k = \frac{\langle F_2 \rangle}{2\langle Q(\kappa_c, d) \rangle} \Gamma \left[-1/3, \frac{2\nu k_c^2}{3|\tilde{a}|} \right]. \tag{2.2}$$

Here $\langle \rangle$ denotes an averaging strategy, presently computed as the arithmetic mean of 26 neighbouring points (Chung & Pullin 2009). The quantity F_2 is the second-order velocity structure function of the resolved-scale velocity field, $k_c = \pi/\Delta_c$ is the cutoff wavenumber with Δ_c the nominal filtering length defined in terms of the local mesh scale, $d = r/\Delta_c$ with r the distance from a neighbour point to the vortex axis (Voelkl *et al.* 2000) and $\Gamma[\cdot\cdot]$ denotes the incomplete gamma function. Additionally, the integral $Q(\kappa_c, d)$ is a model parameter calculated using an asymptotic approximation (Chung & Pullin 2009) and $\tilde{a} = \boldsymbol{e}_i^v \boldsymbol{e}_j^v \widetilde{S}_{ij}$ is the stretch along the subgrid vortex with $\widetilde{S}_{ij}$ the resolved-scale, rate-of-strain tensor. The $\boldsymbol{e}_i^v$ is the local SGS vortex orientation, presently modelled as aligned with the principal extensional eigenvector of $\widetilde{S}_{ij}$.

The main physical model parameters are determined dynamically and locally. Neither line nor plane averaging in homogeneous directions is required and explicit filtering is not used. The model contains an explicit recognition of the true fluid viscosity and is designed to smoothly cutoff in the limit of refining the grid to DNS resolution at a given Reynolds number. Detailed accounts of the SV SGS model and its implementation for incompressible flow are given by Chung & Pullin (2009) and Cheng, Pullin & Samtaney (2015), Cheng *et al.* (2017).

2.3. *Main LES performed*

A sketch of the grooved cylinder is shown in figure 1. It is generated by imposing sinusoidal-shaped grooves on a smooth cylinder so that its radius $R(\theta)$ is given by

$$R = \frac{D}{2} + \frac{\epsilon}{2} \sin \left(2\pi \frac{\mathrm{mod}\,(i-1, N_\theta/k) + N_s}{N_\theta/k} \right) \tag{2.3}$$

and its Cartesian coordinates are

$$x = R \cos \left(2\pi \frac{i-1}{N_\theta} \right), \quad z = R \sin \left(2\pi \frac{i-1}{N_\theta} \right). \tag{2.4a,b}$$

Here i is the mesh index $i = 1 \ldots N_\theta$, where N_θ is the total number of mesh points in the circumferential direction θ. In (2.3) there are three free parameters, the peak to trough height of each groove ϵ, the total number of grooves along the circumferential direction k, and the phase shift parameter to control the groove peak placement with respect to the nominal forward stagnation point N_s. Some testing of the effect of N_s was performed (not shown) by using three different values; $N_s = -N_\theta/(4k)$ which sets the (nominal) front stagnation point at the valley of a groove, $N_s = N_\theta/(4k)$ where the front stagnation point is the peak of a groove, and $N_s = 0$. Presently, $N_s = 0$ is used for all cases.
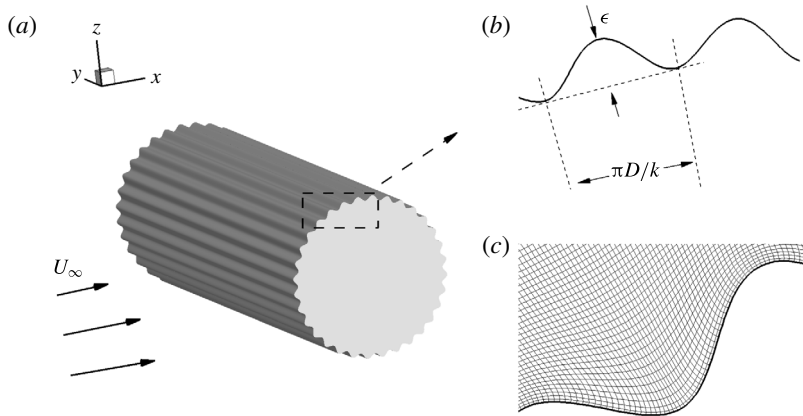
FIGURE 1. Sketch of the simulation geometry. (*a*) Three-dimensional grooved cylinder with inflow U_∞. (*b*) Part of the grooved surface of the cylinder with k the wavenumber and ϵ the magnitude. (*c*) Sketch of the body-fitted curvilinear mesh.

Case	Re_D	k	ϵ/D	L_r/D	L_y/D	N_θ	N_r	N_y
C0	3.9×10^3	32	0	50	3	512	512	128
C1	3.9×10^3	32	1/640	50	3	512	512	128
C2	3.9×10^3	32	1/320	50	3	1024	512	128
C3	3.9×10^3	32	1/160	50	3	1024	512	128
C4	3.9×10^3	32	1/80	50	3	1024	512	256
C5	3.9×10^3	32	1/32	50	3	2048	512	256
C6	3.9×10^3	32	1/16	50	3	2048	512	256

TABLE 2. LES performed for $Re_D = 3.9 \times 10^4$ with increasing ϵ/D. L_r is the computational domain scale in the r direction; L_y is the scale in the spanwise direction; N_θ is the mesh size in the θ direction; N_r is the mesh size in the r direction; N_y is the mesh size in the spanwise direction.

Selection of k is made by referring to available experimental configurations. In experiments by Yamagishi & Oki (2004), 32 grooves are distributed around the cylinder. This distribution of grooves, both triangular and arc shapes, shows a drag decrease for Re_D between 10^4 and 4×10^4. At higher Re_D, the drag coefficient rebounds and reaches a plateau around $Re_D = 5 - 6 \times 10^4$ which indicates that the flow is in a transcritical regime. In Achenbach & Heinecke (1981), 36 groups of R3DP perturbations were used, showing a drag decrease at approximately 3×10^4. Following these experiments, we choose $k = 32$ for all cases.

Achenbach & Heinecke (1981) employed $\epsilon/D \approx 0.032$ for R3DP perturbations while Yamagishi & Oki (2004) adopted $\epsilon/D \approx 0.011$ for both arc and triangle spanwise grooves. Presently, we use several different ϵ/D, from 1/640 to 1/32. First, LES with different ϵ/D at a fixed Re_D are described to investigate how the grooved-cylinder flow gradually deviates from the canonical smooth-wall cylinder flow. Then, we fix a relatively large groove height in order to study the flow behaviour with varying Re_D.

A summary of main cases implemented is given in three tables. In table 2, six cases with fixed $Re_D = 3.9 \times 10^3$ and $k = 32$ are shown, with different ϵ/D: 0, 1/640, 1/320, 1/160, 1/80 and 1/32 respectively. Cases in table 3 have varying Re_D with

Case	Re_D	k	ϵ/D	L_r/D	L_y/D	N_θ	N_r	N_y
C5	3.9×10^3	32	1/32	50	3	2048	512	256
D5	1.0×10^4	32	1/32	50	3	2048	512	256
E5	2.0×10^4	32	1/32	50	3	2048	512	256
E5-2	2.0×10^4	32	1/32	50	3	1024	512	128
F5	4.0×10^4	32	1/32	50	3	2048	512	256
G5	5.0×10^4	32	1/32	50	3	2048	512	256
H5	6.0×10^4	32	1/32	50	3	2048	512	256

TABLE 3. LES performed for $k = 32$, $\epsilon/D = 1/32$ with varying Re_D. Case E5-2 is specially for mesh verification, results shown in appendix A.

Case	Re_D	k	ϵ/D	L_r/D	L_y/D	N_θ	N_r	N_y
C4	3.9×10^3	32	1/80	50	3	1024	512	256
D4	1.0×10^4	32	1/80	50	3	1024	512	256
E4	2.0×10^4	32	1/80	50	3	1024	512	256
F4	5.0×10^4	32	1/80	50	3	1024	512	256

TABLE 4. LES performed for $k = 32$, $\epsilon/D = 1/80$ with varying Re_D.

Case	Re_D	k	ϵ/D	L_r/D	L_y/D	N_θ	N_r	N_y
B0	3.9×10^3	64	1/32	50	3	2048	512	128
B1	8×10^3	64	1/32	50	3	2048	512	128
B2	1×10^4	64	1/32	50	3	2048	512	128
B3	1.5×10^4	64	1/32	50	3	2048	512	256
B4	2×10^4	64	1/32	50	3	2048	512	256
B5	3×10^4	64	1/32	50	3	2048	512	256

TABLE 5. LES performed for $k = 64$, $\epsilon/D = 1/32$ and varying Re_D.

fixed $k = 32$ and $\epsilon/D = 1/32$. We use Re_D up to 6×10^4, which as shown later, is believed to reach the lower transcritical regime. These are the two main LES sets discussed in detail. Table 4 shows an additional set with $\epsilon = 1/80$ for which we show some mean-flow properties. In the tables, we list the computational domain size in the r direction L_r, the computational size in the spanwise direction L_y and the mesh sizes in the θ, r and spanwise y directions respectively for all cases. Sketches of the computational domain in the (x, y) plane are shown in figure 2. In figure 2(*a,b*), we show reduced mesh images for case 'C5' but, for clarity, with every eighth point in the θ direction and every second point in the r direction displayed. The stretching along the r direction can be clearly seen. The grid stretching strategies for different cases is similar that used by Cheng *et al.* (2017). A brief discussion of near-wall resolution requirements for wall-resolved LES, and how these are satisfied, is given in appendix A. Mesh independence for different circumferential and spanwise mesh resolutions, is also demonstrated in appendix A by comparing the wall-parallel velocity at several locations for LES at $Re_D = 2 \times 10^4$ for two different meshes.
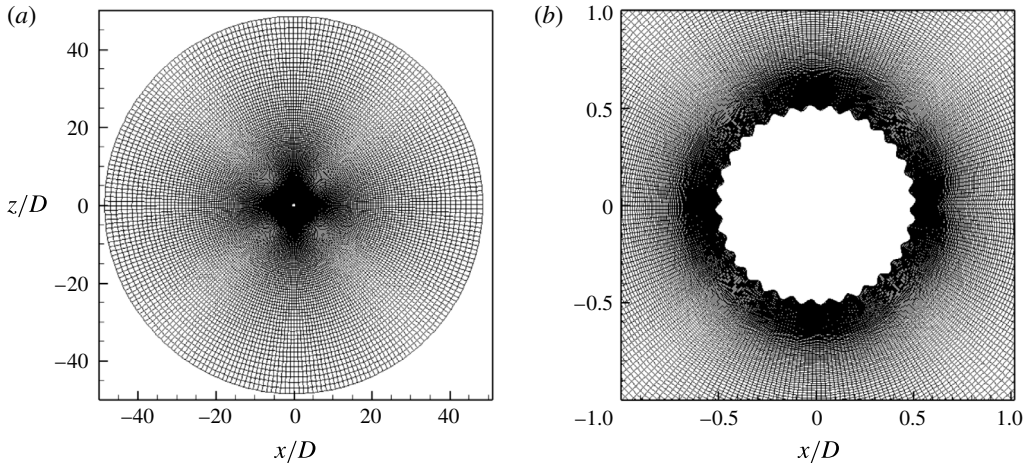
FIGURE 2. Sketch of computation domain: (*a*) full domain; (*b*) close-up around the grooved cylinder.

3. Mean-flow results at $Re_D = 3.9 \times 10^3$

We begin with $Re_D = 3.9 \times 10^3$, which is a well-documented case in the subcritical regime. We compare flow over grooved cylinders with increasing groove height to smooth-cylinder flow with increasing Re_D. In comparison, we note that the flow over a smooth cylinder in the subcritical regime has several documented tendencies with increasing Re_D. An important parameter is the length of the mean-flow recirculation bubble, which is believed to be monotonically decreasing with Re_D in the subcritical regime (Breuer 2000). Another tendency refers to the azimuthal distribution of the pressure coefficient C_p, which exhibits a near-constant minimum value followed by a plateau for $Re_D > 10^4$; see Weidman (1968). Thus, the integration of C_p, which is the dominant component of drag coefficient C_D, is also nearly constant with Re_D for this Re_D range. Additionally, we will also discuss the behaviour of the skin-friction coefficient produced by the groove undulations.

3.1. *Length of the mean-flow recirculation bubble L_B*

In the flow over a cylinder, the two symmetric primary separations comprise a mean-flow recirculation bubble just downstream of the cylinder. The length of this recirculation bubble, L_B, is an important statistic for near-wake flow. An experimental estimate of L_B for the smooth-cylinder flow at $Re_D = 3.9 \times 10^3$ can be interpolated from experiments by Cardell (1993). This gives $L_B/D = 1.33 \pm 0.2$. The present LES of smooth-cylinder flow shows similar results with $L_B/D = 1.31$, which also agrees well with LES results by Kravchenko & Moin (2000). For the flow over a grooved cylinder, the bubble generally shrinks with increasing ϵ/D, as shown in figure 3 which depicts a comparison of the smooth cylinder flow case and the strongly grooved cylinder case with $\epsilon/D = 1/32$. It is found that the length of the separation bubble in figure 3(*b*) is approximately $L_B/D = 0.8$. For completeness we plot L_B/D for all C cases in figure 4. A monotonic decreasing tendency with increasing ϵ/D can be observed. For large amplitude grooves L_B/D appears to approach an asymptotic constant value.
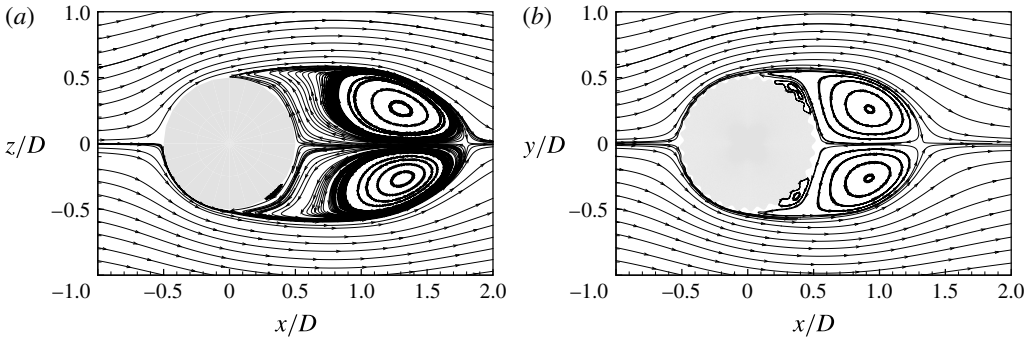
FIGURE 3. Streamlines of mean velocity in Cartesian coordinates: (*a*) $\epsilon/D = 0$, smooth case; (*b*) $\epsilon/D = 1/32$.
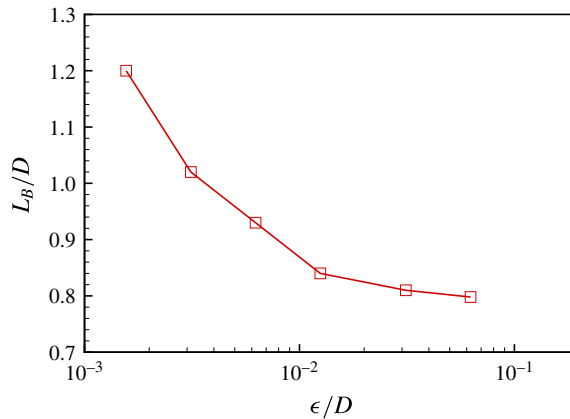

FIGURE 4. (Colour online) The length of the recirculation bubble for $Re_D = 3900$ and varying ϵ/D.

3.2. *Pressure coefficient C_p*

The pressure coefficient C_p is the most important parameter from an engineering viewpoint as it contributes to the dominant part of the total drag. Except where otherwise specified, we subsequently plot mean-flow surface profiles against θ, which monotonically increases along the cylinder surface from front to rear. In flow over the smooth cylinder, starting from the front stagnation point, C_p monotonically decreases up to approximately $\theta = 70°$, reaches a minimum value then rebounds back. In flow over the grooved cylinder, owing to the kinks on the surface, C_p shows a local complex structure on each groove, as shown in figure 5. Also shown in figure 5 is a sketch of the surface profile projected along the θ direction. We can perceive the filtered (over the waves) global variation of C_p, which is similar to the smooth-cylinder flow, decreasing from the front stagnation point in the unit of each groove, reaching a minimum and then rebounding back. The small-scale structure on the groove scale also shows variation depending on the groove's azimuthal location. On the front side of the cylinder, the structure becomes increasingly intense along the θ direction. Once primary mean-flow separation takes place, C_p shows a much flattened plateau, even for the most strongly grooved case with $\epsilon/D = 1/16$. It is
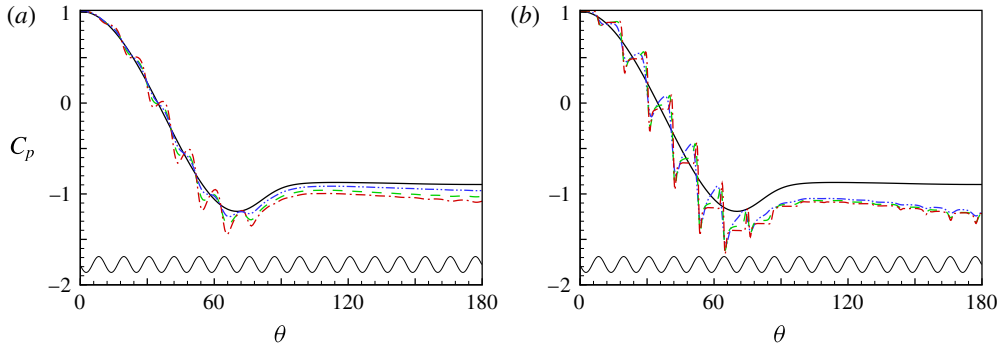
FIGURE 5. (Colour online) Pressure coefficient C_p for $Re_D = 3900$ and varying ϵ/D: ——, smooth case. (a) — $\cdot\cdot$ —, $\epsilon/D = 1/640$; $----$, $\epsilon/D = 1/320$; — $\cdot$ —, $\epsilon/D = 1/160$. (b) — $\cdot\cdot$ —, $\epsilon/D = 1/80$; $----$, $\epsilon/D = 1/32$; — $\cdot$ —, $\epsilon/D = 1/16$.
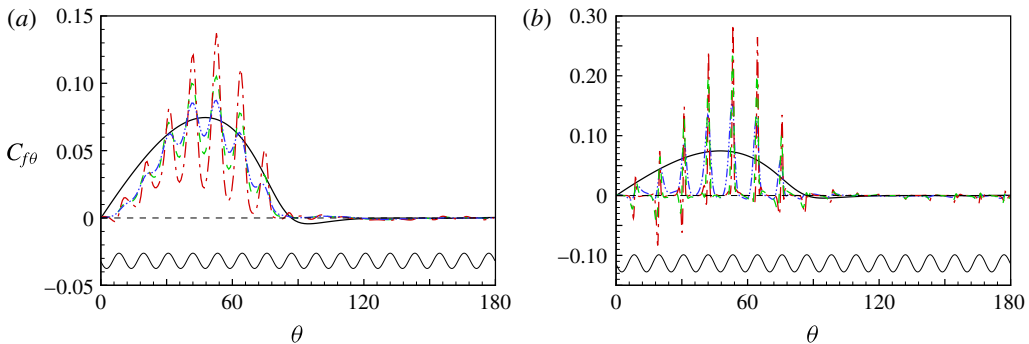
FIGURE 6. (Colour online) Skin-friction coefficient $C_{f\theta}$ for $Re_D = 3900$ and varying ϵ/D: ——, smooth case. (a) — $\cdot\cdot$ —, $\epsilon/D = 1/640$; $----$, $\epsilon/D = 1/320$; — $\cdot$ —, $\epsilon/D = 1/160$. (b) — $\cdot\cdot$ —, $\epsilon/D = 1/80$; $----$, $\epsilon/D = 1/32$; — $\cdot$ —, $\epsilon/D = 1/16$.

interesting that the two high ϵ/D cases give similar minimum and plateau values. This feature is also seen in the flow over a smooth cylinder where high Re_D cases within the subcritical regime give similar plateau values; see the experimental data of Weidman (1968) and the LES results of Cheng *et al.* (2017).

3.3. *Skin-friction coefficient $C_{f\theta}$*

The mean-flow skin-friction coefficient $C_{f\theta} \equiv \overline{\tau_{f\theta}}/(0.5\,\rho\,U_\infty^2)$ in the grooved-cylinder cases deviates substantially from that in the smooth-wall case. We presently define $C_{f\theta}$ (and $\overline{\tau_{f\theta}}$) as that component of the mean skin-friction-vector coefficient on the cylinder surface that lies in the direction perpendicular to the spanwise coordinate. That is, the component along the grooved wall in a cut at constant y. In figure 6, $C_{f\theta}(\theta)$ for the six grooved cases are compared with the smooth-wall case. It can be seen that, with increasing ϵ/D, $C_{f\theta}$ tends to show rapid variation on each groove. For cases up to $\epsilon/D = 1/320$, this fluctuation is generally around the baseline of $C_{f\theta}$ from the smooth case, not reaching the zero line. Cases with $\epsilon/D = 1/80$ and $1/32$ show strong fluctuations in the θ direction that become negative and then positive indicating locally reversed flow inside local, mean-flow separation bubbles within grooves on
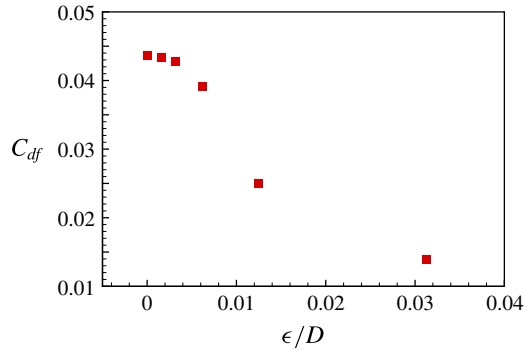
FIGURE 7. (Colour online) Skin-friction drag coefficient C_{df} for $Re_D = 3900$ with varying ϵ/D.

the front part of the cylinder. The drag coefficient due to skin friction, C_{df}, can be obtained from the integral of skin-friction coefficient along the streamwise direction. Figure 7 shows that C_{df} decreases with increasing ϵ/D.

3.4. *Mean-flow field*

The skin-friction coefficient $C_{f\theta}$ reflects the complexity of the separation behaviour. To understand how the flow develops with increasing ϵ/D at $Re_D = 3.9 \times 10^3$, it is useful to plot the streamlines of the mean flow around the separation region.

In figure 8, we plot six cases with $\epsilon/D = 0$, 1/640, 1/160, 1/80 and 1/32. In the figures, we use letters to indicate the flow state inside each groove: '*N*' for attached flow, '*C*' for a trapped (mean-flow) separation bubble with clockwise direction, '*A*' for a trapped separation bubble with anti-clockwise direction, '*P*' denoting the position of the primary mean-flow recirculation bubble, and '*S*' representing the larger-scale secondary separation bubble.

Figure 8(*a*) is for $\epsilon/D = 0$ which corresponds to the smooth-cylinder case. A secondary separation bubble on the leeward surface of the cylinder downstream of primary separation can clearly be seen. For $\epsilon/D = 1/640$ as shown in figure 8(*b*), there is no separated flow on the front part of the cylinder. Downstream of the primary separation point, a secondary separation bubble exists, while further downstream, a tiny anti-clockwise bubble emerges. For $\epsilon/D = 1/160$ (figure 8*c*), a tiny clockwise bubble can be observed just upstream of primary separation.

When ϵ/D is increased to 1/80 in figure 8(*d*), all grooves inside the view on the windward surface exhibit groove-scale separated flow. For deep grooves with $\epsilon/D = 1/32$, there is an anti-clockwise bubble at approximately $x = 0.1$, which is the primary separation bubble in the above two cases. This is clearly evidence of the tendency for the secondary separation bubble to move upstream as ϵ/D is increased. For the deepest grooves in the present study with $\epsilon = 1/16$, figure 8(*f*) shows similar types of bubbles as for $\epsilon = 1/32$, which include clockwise bubbles on the windward surface, followed by the initiation of primary separation, an anti-clockwise bubble and a global secondary separation bubble successively.
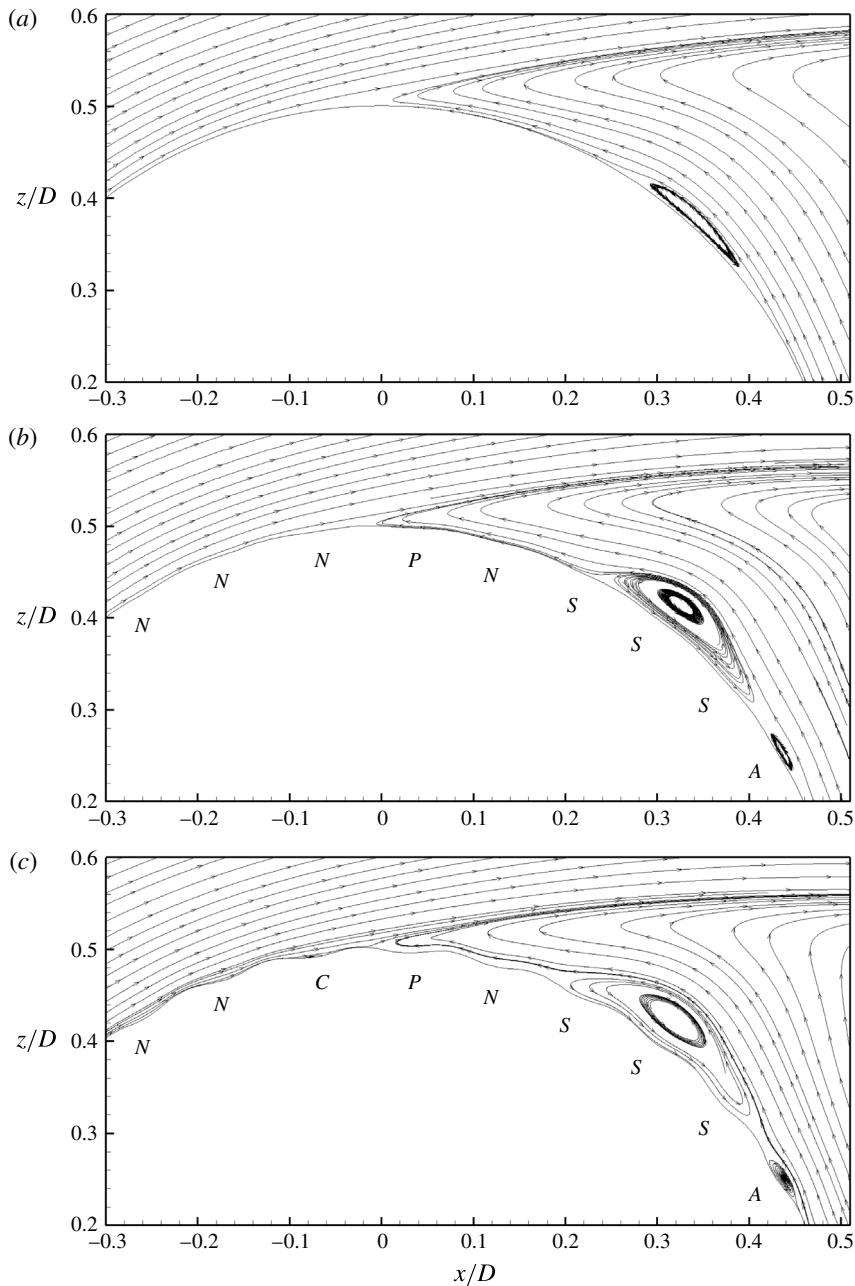
(a)

(b)

(c)

FIGURE 8. For caption see next page.

3.5. *Non-dimensional pressure gradient parameter β*

The non-dimensional pressure gradient parameter β is defined as

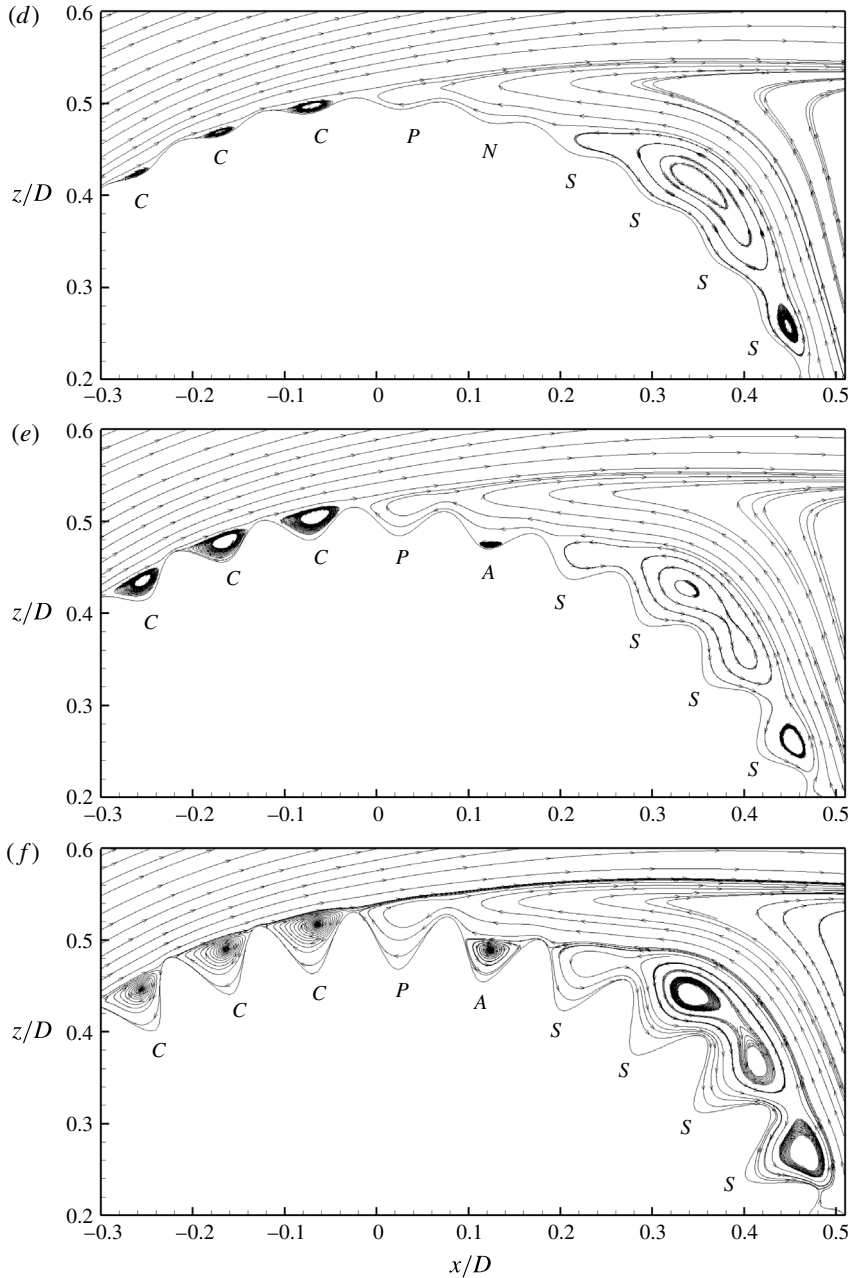$$\beta \equiv \frac{\delta^*}{u_\tau^2} \frac{\mathrm{d}p}{\mathrm{d}\theta},$$

(3.1)

FIGURE 8. (cntd). Local streamlines of mean velocity around the separation region with $Re_D = 3.9 \times 10^3$: (*a*) $\epsilon/D = 0$; (*b*) $\epsilon/D = 1/640$; (*c*) $\epsilon/D = 1/160$; (*d*) $\epsilon/D = 1/80$; (*e*) $\epsilon/D = 1/32$; (*f*) $\epsilon/D = 1/16$.

where δ^* is the displacement boundary-layer thickness, u_τ the local wall friction velocity and $dp/d\theta$ the pressure gradient. This is an important parameter characterizing boundary-layer flow in the presence of a pressure gradient. For the smooth-walled cylinder flow, the distribution of $\beta(\theta)$ over the attached flow portion of the cylinder
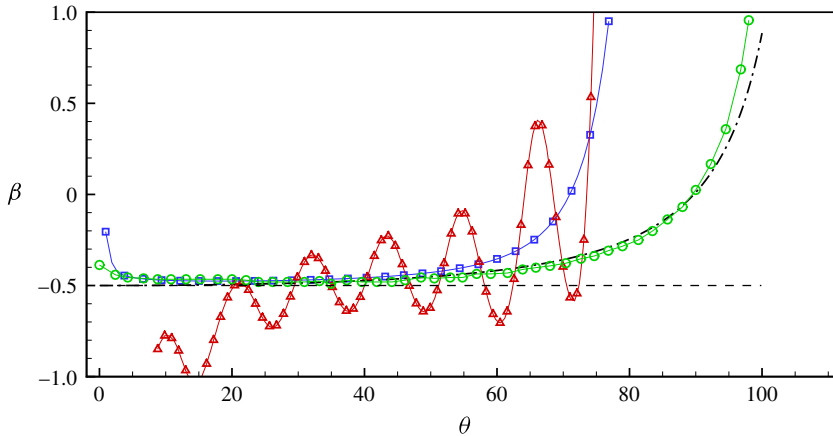
FIGURE 9. (Colour online) Non-dimensional pressure gradient parameter β: $\square$, $Re_D = 3.9 \times 10^3$ for smooth cylinder; $\bigcirc$, $Re_D = 8.5 \times 10^5$ for smooth cylinder; — $\cdot$ —, estimate using the Thwaites (1949) method for smooth-wall case with outer potential flow; $\triangle$, $Re_D = 3.9 \times 10^3$, $k = 32$ and $\epsilon/D = 1/640$ for grooved cylinder.

surface can be estimated using the Thwaites (1949) method. This is done in appendix B, where it is shown that β is nearly constant on the front part of the smooth cylinder, up to $\theta \approx 60°$. LES results from Cheng *et al.* (2017) for the smooth-wall case are compared with this estimate in figure 9, where a subcritical flow with $Re_D = 3.9 \times 10^3$ and a supercritical flow with $Re_D = 8.5 \times 10^5$ are shown. In figure 9, we also plot the present LES of the flow with the smallest groove $\epsilon/D = 1/640$. In computing u_τ^2 and $dp/d\theta$, calculations using the LES results were performed along the actual grooved surface. Since for $\epsilon/D = 1/640$ the flow on the windward part of the cylinder is fully attached, computing of δ^* was implemented along the radial direction. The plot shows oscillatory β owing to the presence of the groove geometry together with substantial deviations from the smooth-cylinder flow.

4. Mean-flow results at high Re_D

The LES at $Re_D = 3.9 \times 10^3$ clearly indicates that with increasing ϵ/D the secondary separation bubble moves upstream. Qualitatively this is similar to the same tendency, when increasing Re_D, within the subcritical regime for smooth-cylinder flow. We now fix $\epsilon/D = 1/32$ and investigate the flow behaviour at different Re_D.

4.1. *The pressure coefficient C_p*

In figure 10, we show the C_p distribution for $Re_D = 3.9 \times 10^3$, 2×10^4 and 5×10^4. Compared to $Re_D = 3.9 \times 10^3$, the minimal pressure coefficient at higher Re_D decreases while the plateau value increases. This effect is stronger for $Re_D = 5 \times 10^4$ than for $Re_D = 2 \times 10^4$, and can be interpreted as evidence that the flow has reached the supercritical regime.

To support our interpretation of the C_p variation, we refer to experiments comparable to the present LES. First we consider a series of experiments on flow past a cylinder with three-dimensional surface geometry perturbations by Achenbach
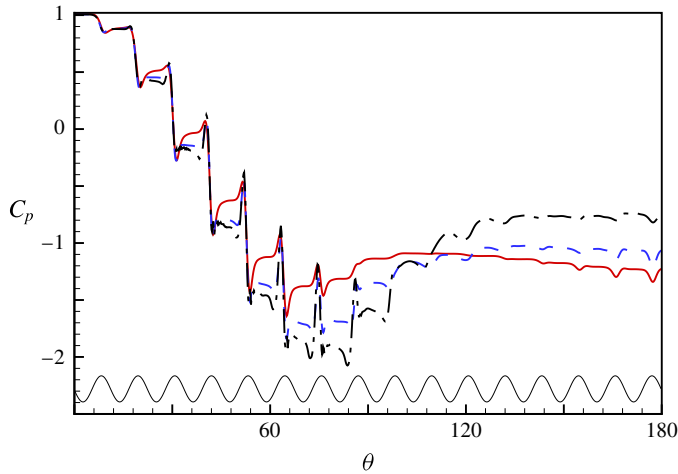
FIGURE 10. (Colour online) Pressure coefficient C_p for $\epsilon/D = 1/32$: ——, $Re_D = 3.9 \times 10^3$; – – – –, $Re_D = 2 \times 10^4$; — $\cdot$ —, $Re_D = 5 \times 10^4$.
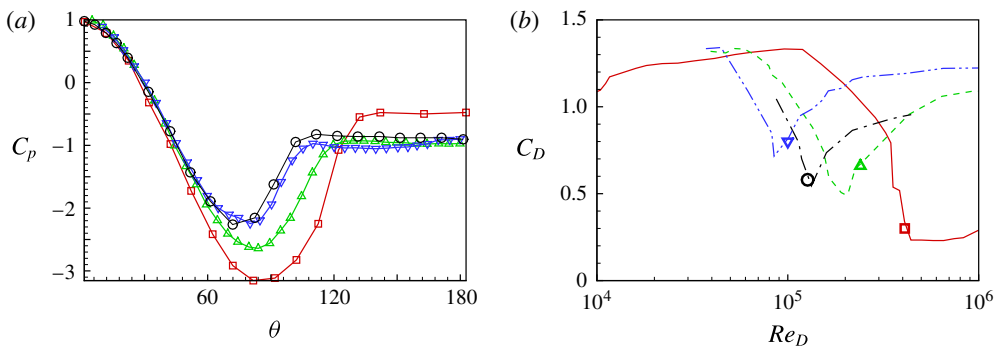

FIGURE 11. (Colour online) Comparison of experimental C_p in the supercritical regime: (*a*) distribution of C_p for four cases; (*b*) location of four cases in a C_D plot. $\square$ (——), $Re_D = 4.1 \times 10^5$, smooth-cylinder flow $\epsilon/D = 0$ (Güven *et al.* 1980); $\triangle$ (– – – –), $Re_D = 2.4 \times 10^5$, $\epsilon/D = 0.7 \times 10^{-3}$ (Achenbach 1971); $\bigcirc$, (— $\cdot$ —) $Re_D = 1.27 \times 10^5$, $\epsilon/D = 1.6 \times 10^{-3}$ (Güven *et al.* 1980); $\triangledown$ (— $\cdot$ $\cdot$ —), $Re_D = 10^5$, $\epsilon/D = 2.9 \times 10^{-3}$ (Achenbach 1971).

(1971), Güven *et al.* (1980) and the R3DP experiments of Achenbach & Heinecke (1981). In these experiments, different magnitudes of perturbation are studied. To understand the supercritical behaviour in these flows, we collect four C_p plots, as shown in figure 11(*a*). In figure 11(*b*), C_D corresponding to the respective C_p distributions are located on a C_D-Re_D plot showing four curves from the respective experiments. This shows one point near the beginning of the supercritical regime for the smooth-cylinder case and three points just above their minimal C_D for different wavy shapes. To identify the different perturbations, here we use ϵ/D, which is the ratio of the height of the perturbations to the diameter of the cylinder. The three lines represent $\epsilon/D = 0.7 \times 10^{-3}$, 1.6×10^{-3} and 2.9×10^{-3} respectively.

In figure 11, the four corresponding C_p distributions are plotted. For the smooth-cylinder case, the minimal value can approach $C_p = -3$, while for the experiments
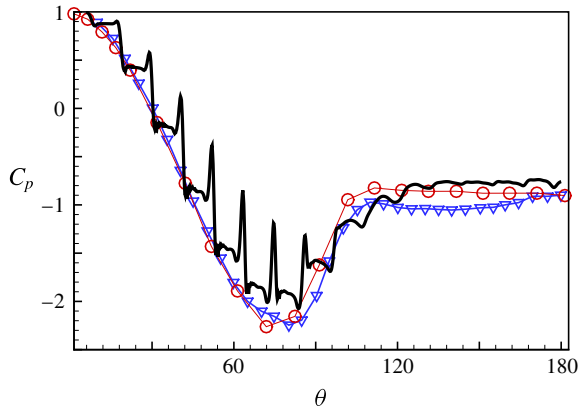
FIGURE 12. (Colour online) Comparison of C_p between LES data and rough-wall experiment: ——, LES at $Re_D = 5 \times 10^4$, $k = 32$ and $\epsilon/D = 1/32$. For legend, see figure 11.
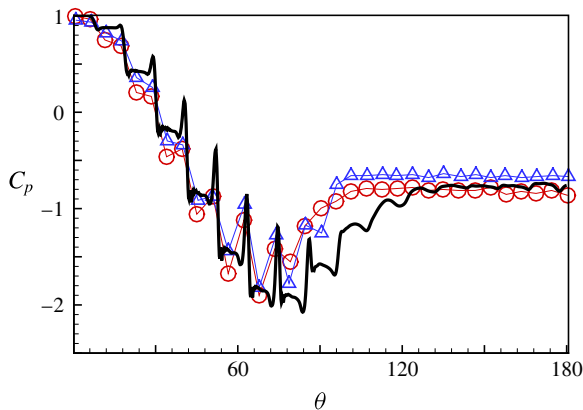

FIGURE 13. (Colour online) Comparison of C_p between LES data and grooved-wall experiment: ——, LES at $Re_D = 5 \times 10^4$, $k = 32$ and $\epsilon/D = 1/32$. Experimental data at $Re_D = 10^5$ by Yamagishi & Oki (2004): ○, arc groove; △, triangle groove.

with three-dimensional geometry perturbations, the minimal value increases substantially. The two higher ϵ/D cases show similar C_p distributions. These same two C_p distributions are also shown in figure 12 in comparison with results from the present LES at $Re_D = 5 \times 10^4$. While the LES are for two-dimensional grooves with $\epsilon/D = 1/32$, the general behaviour of the C_p distributions is similar, including the minimal value of C_p, the increasing tendency from the minimal value to the plateau value and also the plateau value.

We can also compare the present LES with experimental results by Yamagishi & Oki (2004) for flow over a cylinder with two-dimensional grooves, with two different shapes: triangle- or arc-shaped grooves. Experimental data at $Re_D = 10^5$ are compared with present LES calculations at $Re_D = 5 \times 10^4$ in figure 13. This shows good agreement for the front part of the cylinder and for the plateau region. For
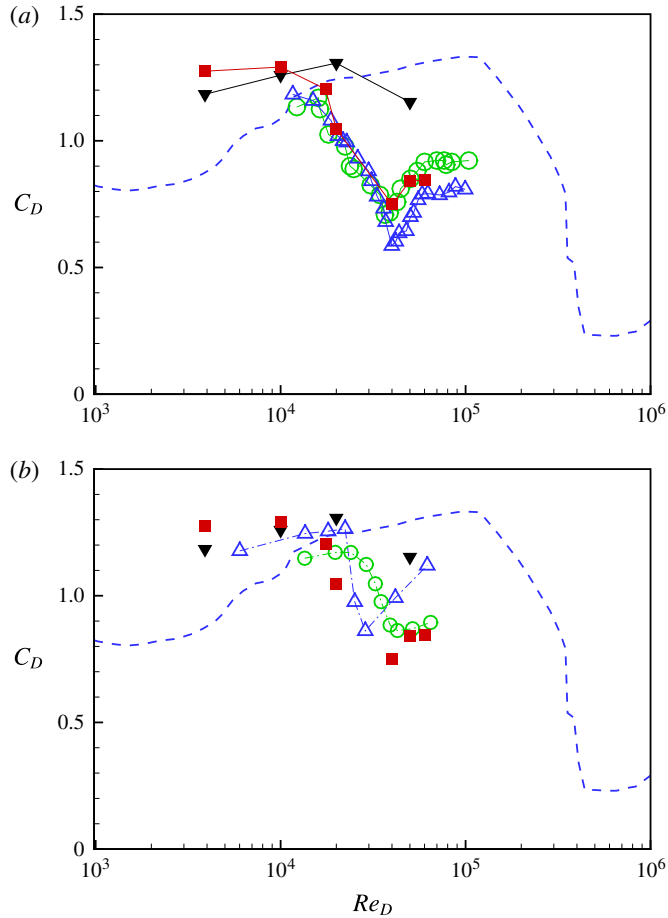
FIGURE 14. (Colour online) Comparison of drag coefficient C_D between LES and experiment: ■, LES with $\epsilon/D = 1/32$, ▼, LES with $\epsilon/D = 1/80$. (a) Experiments of grooved cylinder by Yamagishi & Oki (2004): ○, arc groove; △, triangle groove. (b) Experiments of non-smooth cylinder with 3-D geometric perturbation: △, $\epsilon/D = 0.03$ from experiment with R3DP by Achenbach & Heinecke (1981); ○, $\epsilon/D = 0.02$ from experiment with embedded glass perturbations by Fage & Warsap (1929); − − − −, smooth-wall experiments by Schewe (1983) (for comparison).

the range $50 < \theta < 90°$, both experiments and LES show small structures in each groove and their peaks match each other. We note that there are differences between experiment and LES in $90 < \theta < 120°$. This agrees with our physical interpretation that the present LES at $Re_D = 5 \times 10^4$ reaches the start of the transcritical regime while experimental results at $Re_D = 10^5$ lie well within the transcritical regime.

4.2. *The drag coefficient C_D*

The drag coefficient C_D, which is a combination of integrated pressure and viscous contributions, is shown in figure 14 where LES results are compared with two sets of experimental data. Figure 14(a) shows the two-dimensional groove experiments by Yamagishi & Oki (2004). The present LES with $k = 32$ and $\epsilon/D = 1/32$, generally

follows the experimental data for arc and triangle grooves even though for the latter, $\epsilon/D \approx 0.011$. Also plotted is a third set of LES (table 4) with $k = 32$ and $\epsilon/D = 1/80$, which, at $Re_D = 5 \times 10^4$ lies within the drag crisis, but does not reach the supercritical regime. Figure 14(b) compares C_D for the LES with experimental results for three-dimensional cylinder perturbations, including R3DP by Achenbach & Heinecke (1981) and glass perturbations by Fage & Warsap (1929). Here LES and experiments have similar values of ϵ/D. They show quite similar $C_D - Re_D$ behaviour despite the fact that the LES employs two-dimensional spanwise grooves.

4.3. *Mean-flow field*

From the $C_D - Re_D$ plot, it is clear that for $\epsilon/D = 1/32$, our LES of the flow at $Re_D = 1 \times 10^4$ is still within the subcritical regime, while the flow with $Re_D = 2 \times 10^4$ is in transition to the supercritical regime, and that $Re_D = 5 \times 10^4$ reaches the beginning of the transcritical regime. To understand the role of grooves in the transition, we plot the streamlines of the mean-flow field, with focus on the separated region, as shown in figure 15.

In figure 15(a), we show the streamlines for $Re_D = 3.9 \times 10^3$, which, as described earlier, shows a primary separation at around $x = 0$ and a secondary separation bubble which reattaches at about $x = 0.2$. Upstream of the secondary separation bubble, a small anti-clockwise bubble exists. When Re_D is increased to 8000, as shown in figure 15(b), no obvious change is observed except the growth of the anti-clockwise bubble. With further increase to $Re_D = 10^4$, another anti-clockwise bubble emerges under the separation point of the primary separation bubble, which is labelled as P/A in figure 15(c). The development of anti-clockwise bubbles are signs that the secondary separation bubble, and in particular its mean-flow reattachment line, are moving upstream along the cylinder surface, as Re_D is increased.

A further small increase of Re_D gives a notably different topology. In figure 15(d), we can see that the anti-clockwise bubble, which previously existed just upstream of the secondary separation bubble, is absorbed. The change results in a leapfrogging movement upstream of the reattachment point of the secondary separation bubble, which is now at around $x = 0.1$. This tendency is quite similar to observations from LES of smooth-walled cylinder flows (Cheng *et al.* 2017), where the secondary separation bubble also moves upstream in the subcritical regime, as Re_D is increased.

When transition to supercritical flow occurs, the flow topology changes significantly. With further increase in Re_D, as shown in figure 15(e) for $Re_D = 2 \times 10^4$, the first anti-clockwise trapped bubble still moves forward but now combines with a clockwise trapped bubble (C/A) prior to the primary separation line which labelled as P/A. At this transition Re_D no secondary separation bubble exists. At the same time, all bubbles in the leeward flow are locally trapped with mean-flow anti-clockwise motion (A).

This feature of the flow field at subcritical to supercritical transition is essentially similar to the same phenomena in the smooth-cylinder transition flow. For the latter case Cheng *et al.* (2017) concluded that the change in the mean-flow secondary separation bubble, from anti-clockwise and located within the large-scale separated flow, to a prior, clockwise, separation bubble, is an important mechanism that stimulates the drag crisis. In the present grooved-cylinder flow, owing to strong trapping effects in each groove, the secondary separation bubble gradually shrinks and separates into several anti-clockwise trapped bubbles. This phenomenon cannot occur in the smooth-cylinder flow.
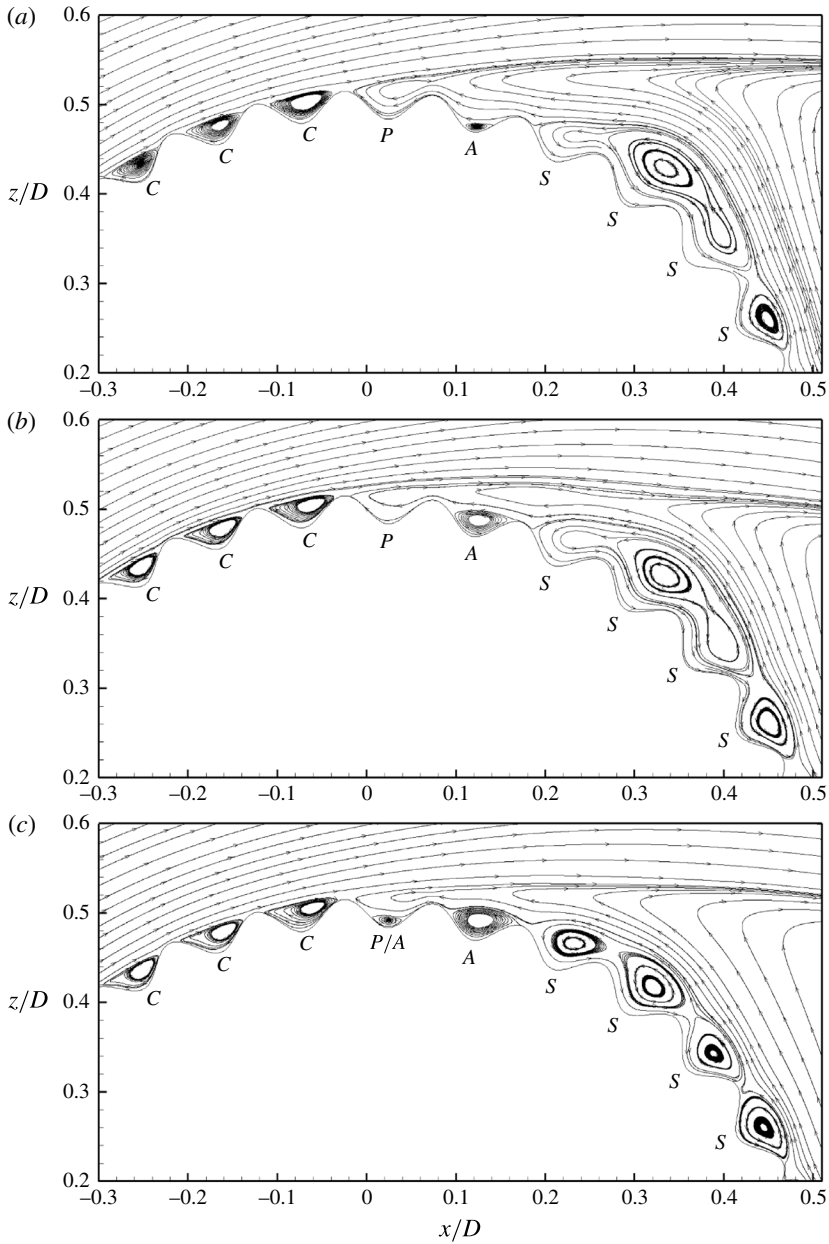
FIGURE 15. For caption see next page.

With further increase in Re_D to $Re_D = 5 \times 10^4$, as shown in figure 15(*c*), the *C/A* structure disappears, and inside all upwind grooves are trapped clockwise bubbles, save possibly for a tiny bubble in the second groove from the left in the figure. For the leeward flow, the *P/A* configuration also disappears and all trapped bubbles flow in an anti-clockwise direction. This perhaps can be interpreted as a signature of the flow having reached the transcritical regime. The analogous criterion for transcritical flow in the smooth-cylinder case is the disappearance of the prior separation bubble (Roshko 1961).
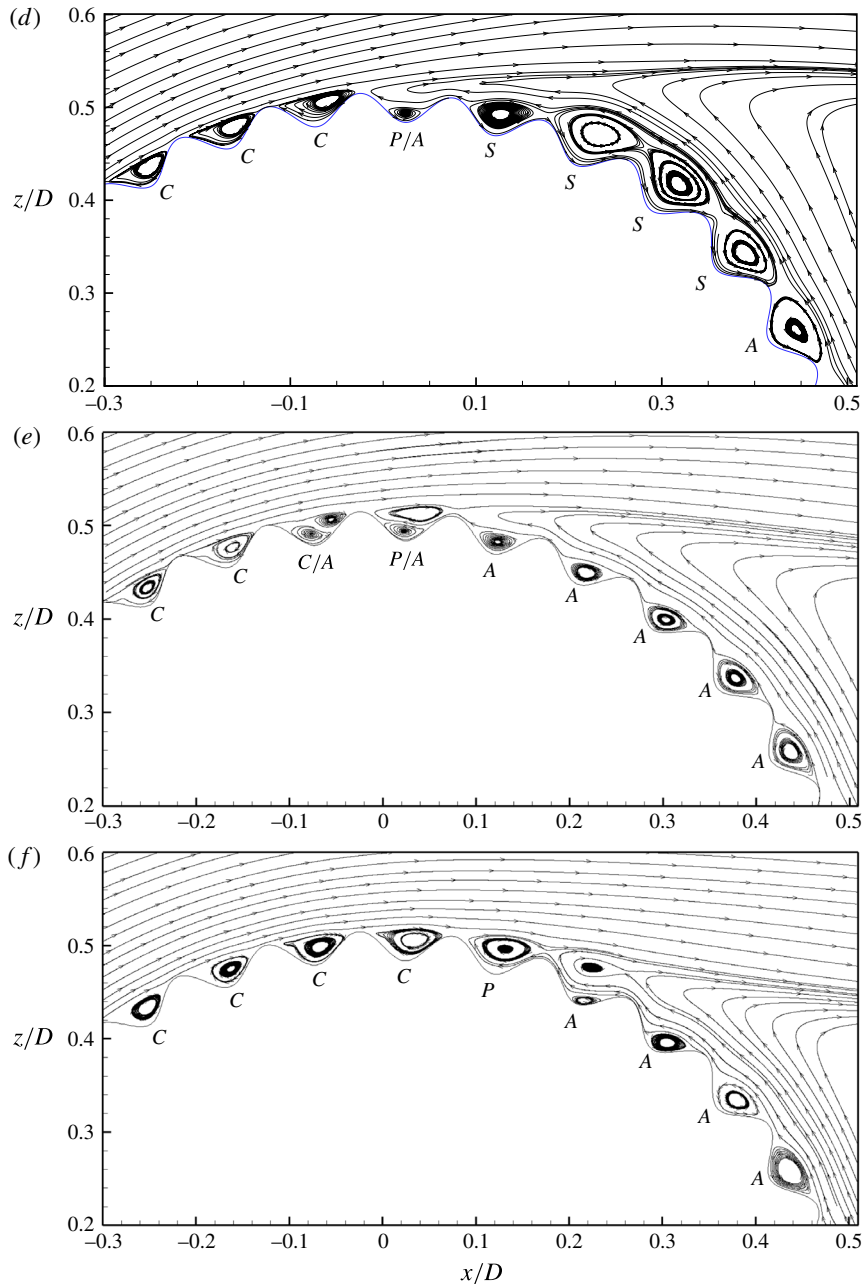
FIGURE 15. (cntd). (Colour online) Local streamlines of mean velocity around the separation region: (*a*) $Re_D = 3.9 \times 10^3$; (*b*) $Re_D = 8 \times 10^3$; (*c*) $Re_D = 1 \times 10^4$; (*d*) $Re_D = 1.05 \times 10^4$; (*e*) $Re_D = 2 \times 10^4$; (*f*) $Re_D = 5 \times 10^4$.

5. Unsteady and instantaneous flow features

In previous sections, mean results of the LES have been discussed together with comparison with available experimental data. Other important flow properties can be
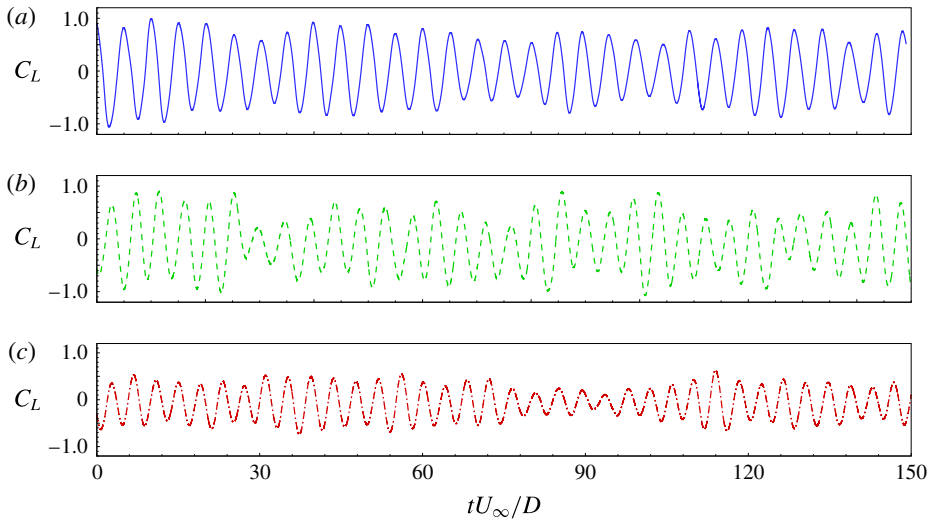
FIGURE 16. (Colour online) History of the lift coefficient C_L for different Re_D: ——,
3.9×10^3; – – – –, 2×10^4; — · —, 5×10^4.

revealed from the tracking of unsteady flow features, for example, the Strouhal number
$St \equiv fD/U_\infty$, where f is the shedding frequency. We now consider unsteady and three-
dimensional flow dynamics via investigation of instantaneous variables, such as the
one-dimensional drag and lift coefficients, two-dimensional vector skin-friction lines
and three-dimensional isoline plots of near-wall flow structures.

5.1. *The instantaneous lift and drag coefficients $C_L(t)$ and $C_D(t)$*

The history of the lift coefficient $C_L(t)$ can be revealing in understanding the
phenomenon of vortex shedding. Schewe (1983) discusses the spectral analysis of
$C_L(t)$ from experimental data, providing evidence for a dominant shedding frequency
around $St = 0.2$ in the subcritical regime, $St = 0.47$ in the supercritical regime,
transition to a sub-region of transcritical regime where no dominant frequency can
be found and a wide spectral content is observed, and then finally to the full
transcritical regime where a dominant frequency of about $St = 0.27$ emerges. The
no-dominant-frequency region was quite ambiguous before the classical experiments
by Roshko (1961). For a non-smooth cylinder, the R3DP experiments of Achenbach
& Heinecke (1981) show no evidence of the existence of a no-dominant-frequency
sub-region of the transcritical regime.

Three $C_L(t)$ time series from the present LES are shown in figure 16, including
$Re_D = 3.9 \times 10^3$, $Re_D = 2 \times 10^4$ and $Re_D = 5 \times 10^4$. While f and the magnitude of the
$C_L(t)$ oscillations vary with Re_D, the general trend of the $C_L(t)$ variation is similar for
all cases. The Strouhal number St versus Re_D is shown in figure 17 in comparison
with the rough-cylinder experiments of Achenbach & Heinecke (1981). All results
generally show a smooth transition from the subcritical regime where $St \approx 0.2$ to the
final transcritical regime where $St \approx 0.25$.

Some insight into the behaviour of $C_L(t)$ in different regimes can be inferred by
observation of the drag coefficient $C_D(t)$. In the experiments by Schewe (1983), for
near-critical-state flow, a secondary frequency can be observed in $C_D(t)$ which interacts
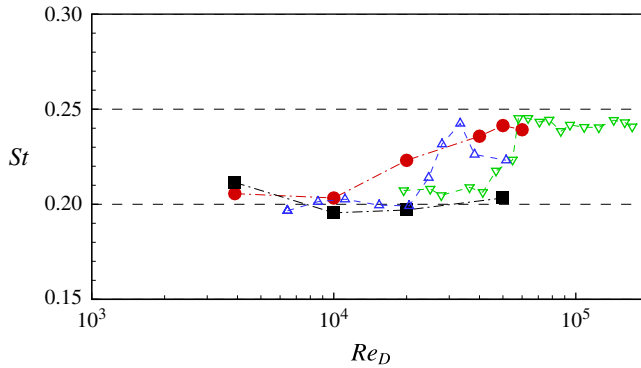with the primary shedding frequency. For the present LES of the grooved-cylinder

FIGURE 17. (Colour online) Strouhal number *St*: comparison of LES ($\bullet$, $\epsilon/D = 1/32$; $\blacksquare$, $\epsilon/D = 1/80$) with experiment of non-smooth cylinder with R3DP by Achenbach & Heinecke (1981) ($\triangle$, $\epsilon/D = 0.03$; $\triangledown$, $\epsilon/D = 0.006$).
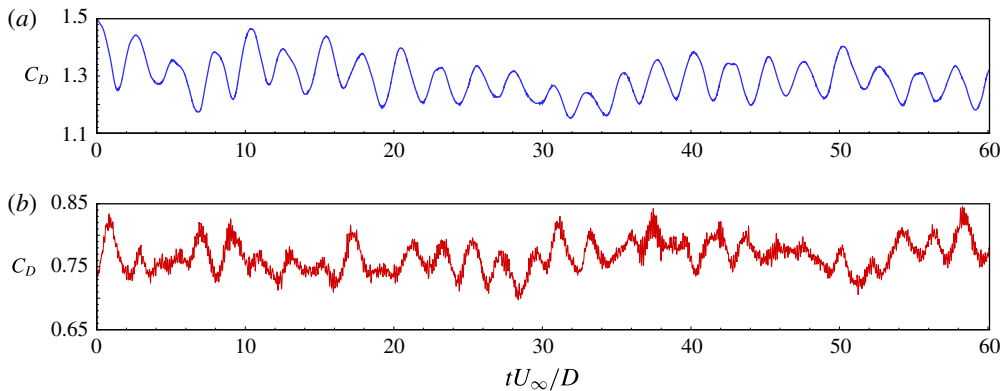

FIGURE 18. (Colour online) History of the drag coefficient C_D: (*a*) $Re_D = 3.9 \times 10^3$; (*b*) $Re_D = 5 \times 10^4$.

flow, a secondary frequency can also be identified at high Re_D, as shown in figure 18. It can be seen that $C_D(t)$ at high Re_D exhibits a high frequency oscillation which is quite distinct from the low frequency that dominates the vortex shedding. This high frequency is generally found to be at approximately 16 times *St*, which indicates that it is mainly produced by the geometrical perturbation of the grooved cylinder. In contrast, for the smooth cylinder flow the presence of wall turbulence possibly generates higher frequency oscillations.

5.2. *Surface skin-friction lines*

The mean flow exists as a two-dimensional projection onto a spanwise normal plane. In order to consider three-dimensional flow effects, we first plot the instantaneous limiting streamlines at the cylinder wall that correspond to the surface skin-friction vector field, or skin-friction lines. These are generally unsteady in that the surface vector field changes as a function of time through shedding cycles. Presently we show typical instantaneous images at an arbitrary time instant. Since the grooved cylinder has a mildly complex surface shape, the present plots will simply project the real
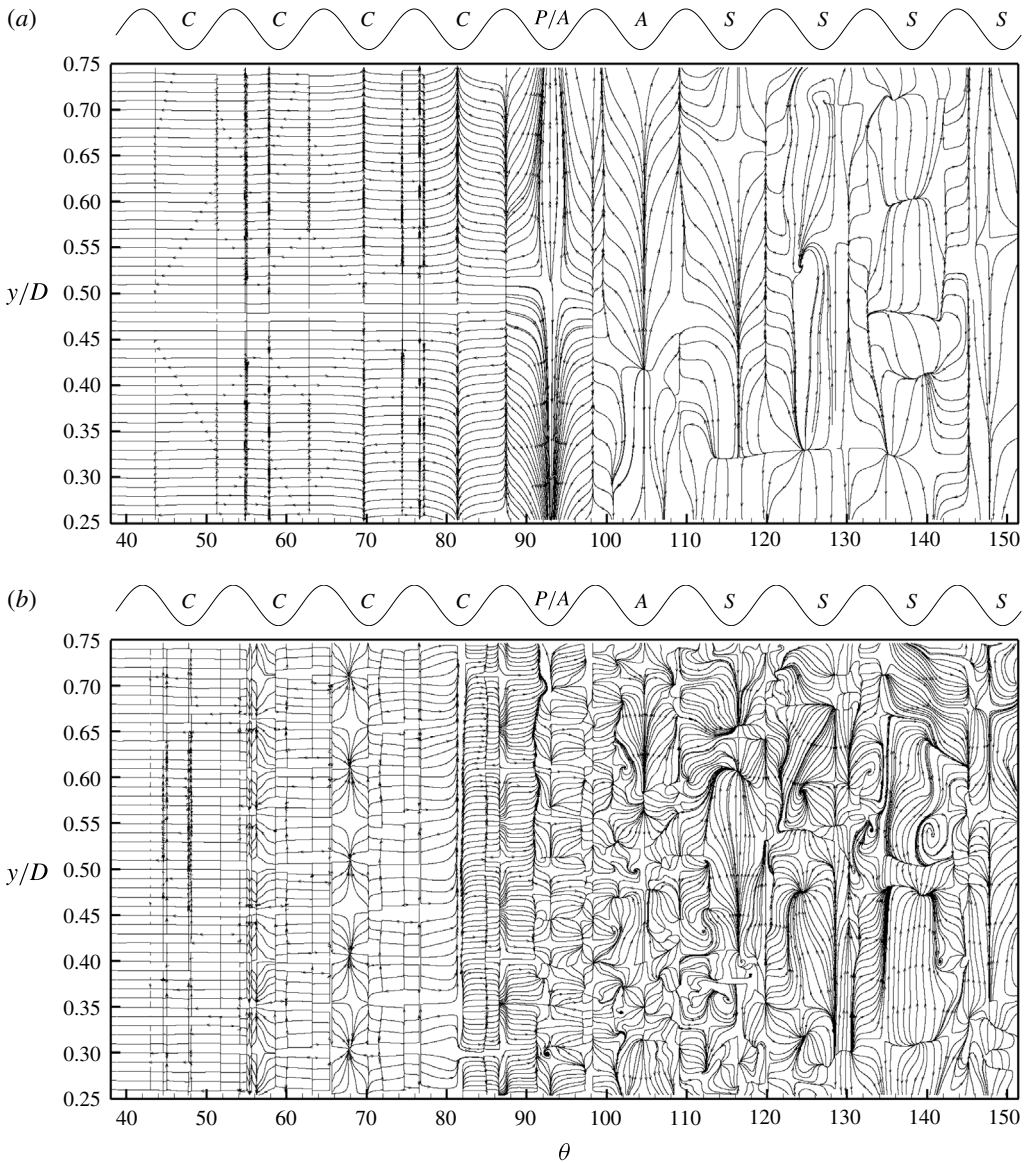
(a)

(b)

θ

FIGURE 19. Instantaneous skin-friction lines of the subcritical regime: (a) $Re_D = 3.9 \times 10^3$; (b) $Re_D = 1.75 \times 10^4$.

skin-friction vectors onto the unperturbed cylinder surface, with (θ, y) as projected surface coordinates.

In figure 19, two portraits of instantaneous surface skin-friction lines in the subcritical regime are shown. The top of each skin-friction line plot indicates both peaks and valleys of grooves and also the corresponding mean-flow groove characteristic as previously denoted by C, A, P and S. In figure 19(a) at $Re_D = 3.9 \times 10^3$, the skin-friction lines upstream of the primary separation region are generally straight lines, which indicates that there is no near-surface spanwise motion. In figure 19(b) for $Re_D = 1.75 \times 10^4$, a two-dimensional surface structure is clearly observed which occupies a scale $\pi/16$ in size in the spanwise direction. This is almost
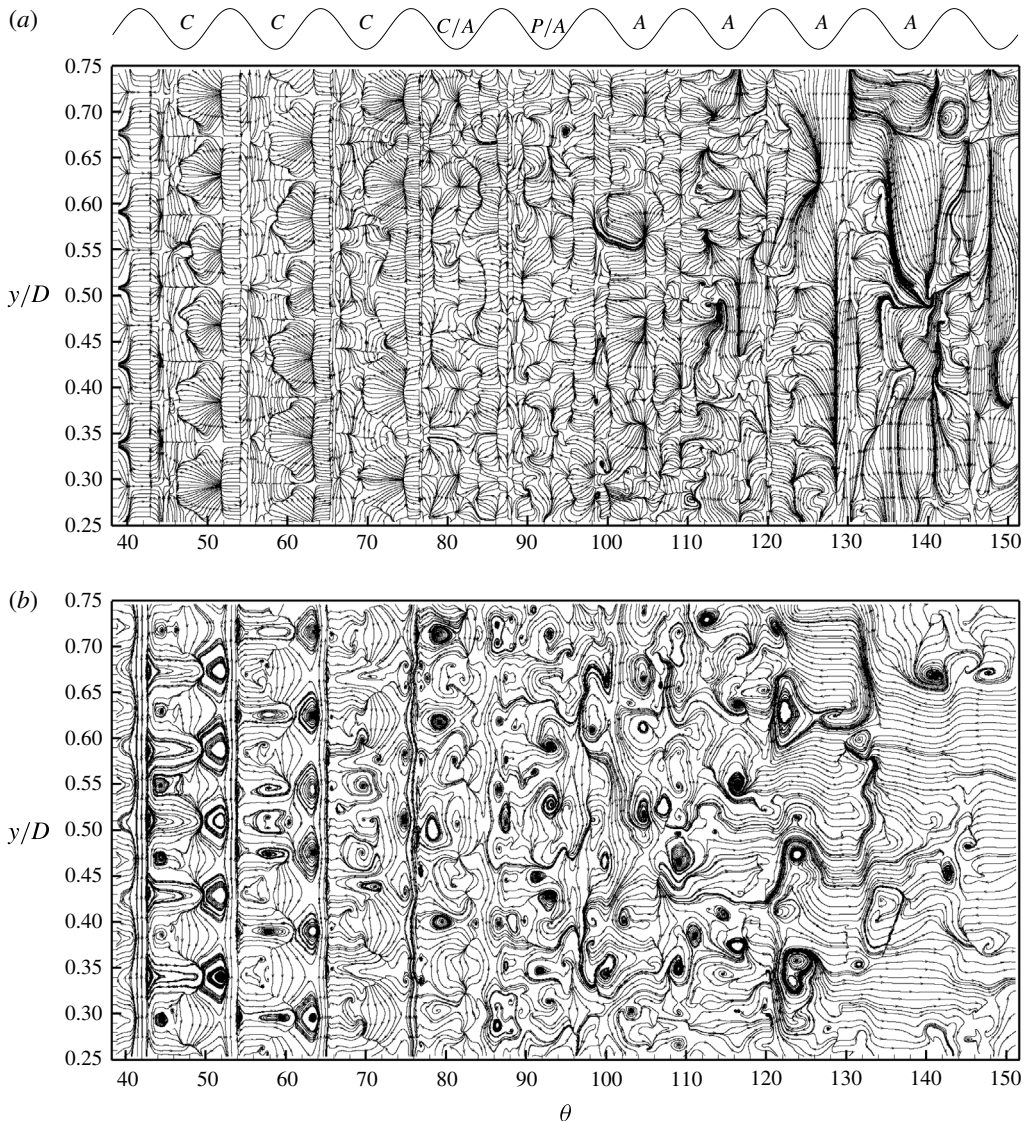
FIGURE 20. $Re_D = 2 \times 10^4$: (*a*) skin-friction lines; (*b*) vortex lines.

the same as the half-wavelength of the groove in the circumferential direction. It is
notable that for both Re_D, skin-friction lines downstream of the primary separation
show substantial spanwise motion indicating a fully three-dimensional flow above.

In figure 20(*a*), a skin-friction portrait for $Re_D = 2 \times 10^4$ is shown. This clearly
shows two-dimensional surface structure, and thus three-dimensional off-wall motion,
even on the very front part of the grooved cylinder. In grooves upstream of the
primary separation, although the mean flow exhibits a clockwise trapped bubble, the
instantaneous skin-friction lines show irregular two-dimensional near-wall flow that
destroys the symmetry in the spanwise direction for the two-dimensional mean-flow
structures. In figure 20(*b*), the surface vortex direction field at the same Re_D is
shown. The surface vortex lines are everywhere orthogonal to the skin-friction lines.
In both images in figure 20, the skin-friction and the surface vortex lines exhibit a
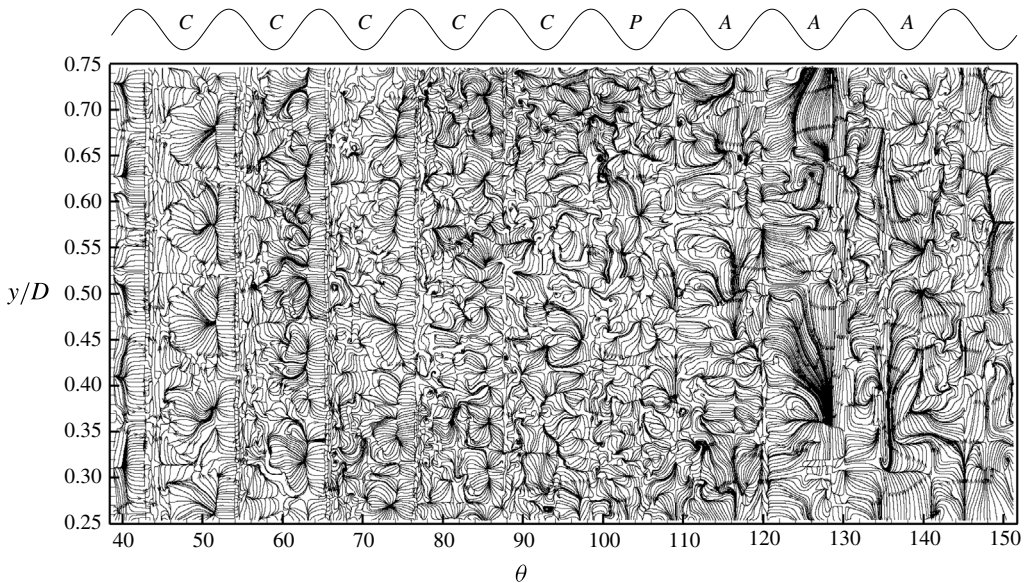
FIGURE 21. Instantaneous skin-friction lines at $Re_D = 5 \times 10^4$.

nearly spanwise-periodic, cell-like structure for the first two grooves shown. Further downstream this breaks down into an irregular spanwise field. Still further downstream in the primary separation bubble region, vortex lines are almost streamwise straight lines. We show skin-friction lines at $Re_D = 5 \times 10^4$ in figure 21. In this case, the breakdown of the two-dimensional surface structure takes place even upstream.

5.3. *Plots of Q-criterion*

In order to visualize instantaneous flow structure away from the wall, we consider the second invariant of the velocity gradient tensor, which is typically defined as Q (see Chakraborty, Balachandar & Adrian 2005)

$$Q = \tfrac{1}{2}(\|\boldsymbol{\Omega}\|^2 - \|\boldsymbol{S}\|^2), \tag{5.1}$$

where $\boldsymbol{S} = 1/2\,(\nabla \boldsymbol{u} + (\nabla \boldsymbol{u})^{\mathrm{T}})$, $\boldsymbol{\Omega} = 1/2\,(\nabla \boldsymbol{u} - (\nabla \boldsymbol{u})^{\mathrm{T}})$ are the rate-of-strain and the rotation tensors respectively. In figure 22 we show instantaneous iso-surfaces of $Q = 1$ coloured by u_x. The four panels use similar Re_D values as for the skin-friction plots of figures 20–26. For the two lower Re_D at 3.9×10^3 and 1.75×10^4, a relatively large near-cylinder domain is shown to illustrate how the flow develops from the boundary-layer flow into the wake. At 3.9×10^3 in figure 22(*a*), the front part of the cylinder shows no variance in the spanwise direction. Only streamwise perturbations, which are induced by the grooves, can be seen. For flow at 1.74×10^4, structure development in the spanwise direction is found to move upstream from the wake and approach the front of the cylinder. In this case, the breakdown of the spanwise uniformity generates some regular structures, which then further interact with the streamwise perturbations and roll finally into the near-wake flow.

In figure 22(*c*) at $Re_D = 2 \times 10^4$, spanwise perturbations are formed at smaller θ than the smaller Re_D flows. With further increase of Re_D to 5×10^4, we can observe in figure 22(*d*) that spanwise regular structures are not apparent and the flow quickly breaks into irregular small scales. As Re_D increases in figure 22, the reduction in the
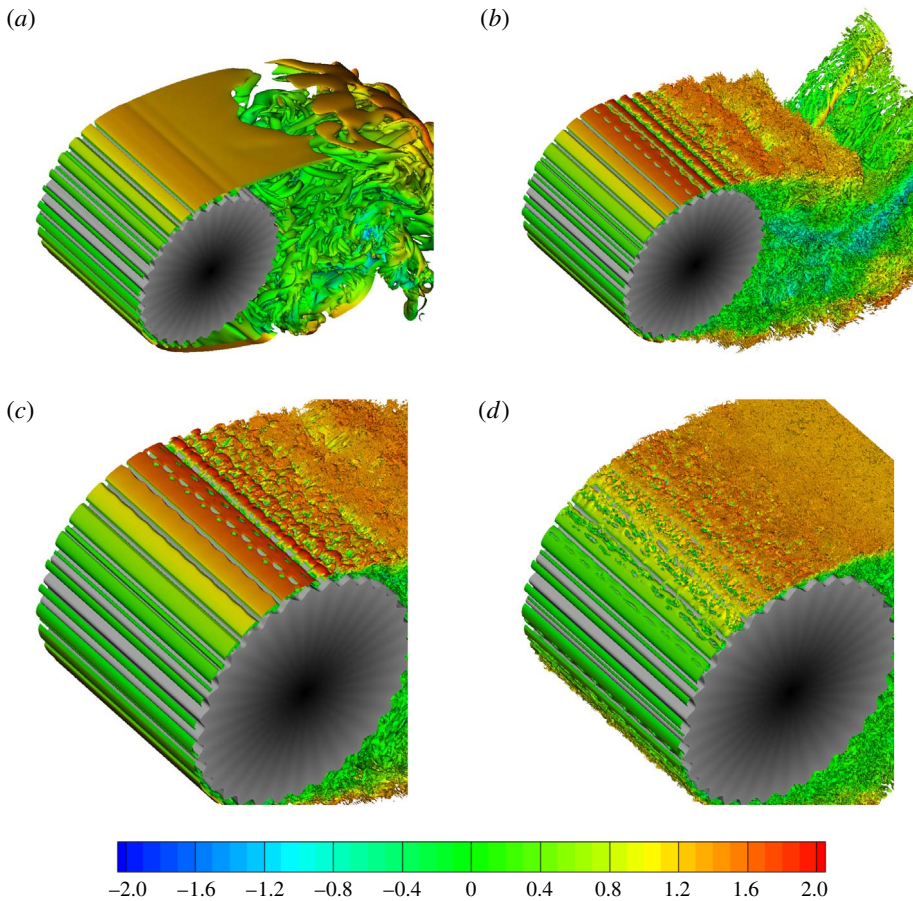
(a)   (b)

(c)   (d)

-2.0	-1.6	-1.2	-0.8	-0.4	0	0.4	0.8	1.2	1.6	2.0

FIGURE 22. Instantaneous flow on the front part of the cylinder. $Q = 1$ and coloured by u_x. (a) $Re_D = 3.9 \times 10^3$; (b) $Re_D = 1.75 \times 10^4$; (c) $Re_D = 2 \times 10^4$; (d) $Re_D = 5 \times 10^4$.

scale of the visible eddies is clear. This is believed to be a genuine Re_D effect and not an artefact of either grid resolution or the visualization scheme. It is interesting to observe that, in the breakdown process of spanwise structures for $Re_D = 2 \times 10^4$, some Λ-shaped vortices emerge, which are similar to the vortices observed in the flat-plate turbulent transition by Sayadi, Hamman & Moin (2013).

While the present work is not a study of the wake dynamics, we nonetheless demonstrate that the present LES does indeed produce a healthy wake structure for the present flow. Full side views using the Q-parameter of streamwise extent up to $13D$ are shown in figure 23 for several different Re_D. It is clear that the present LES and associated mesh structure provides a physically convincing wake flow. A detailed study of the wake flow is beyond the scope of the present work, which is focused on surface and near-surface properties of the flow, and so is not discussed further.

6. Discussion

6.1. *Mean-flow separation angle*

From the previous discussion, a natural question arises concerning the transitions between the subcritical, supercritical and transcritical regimes. In the smooth-cylinder
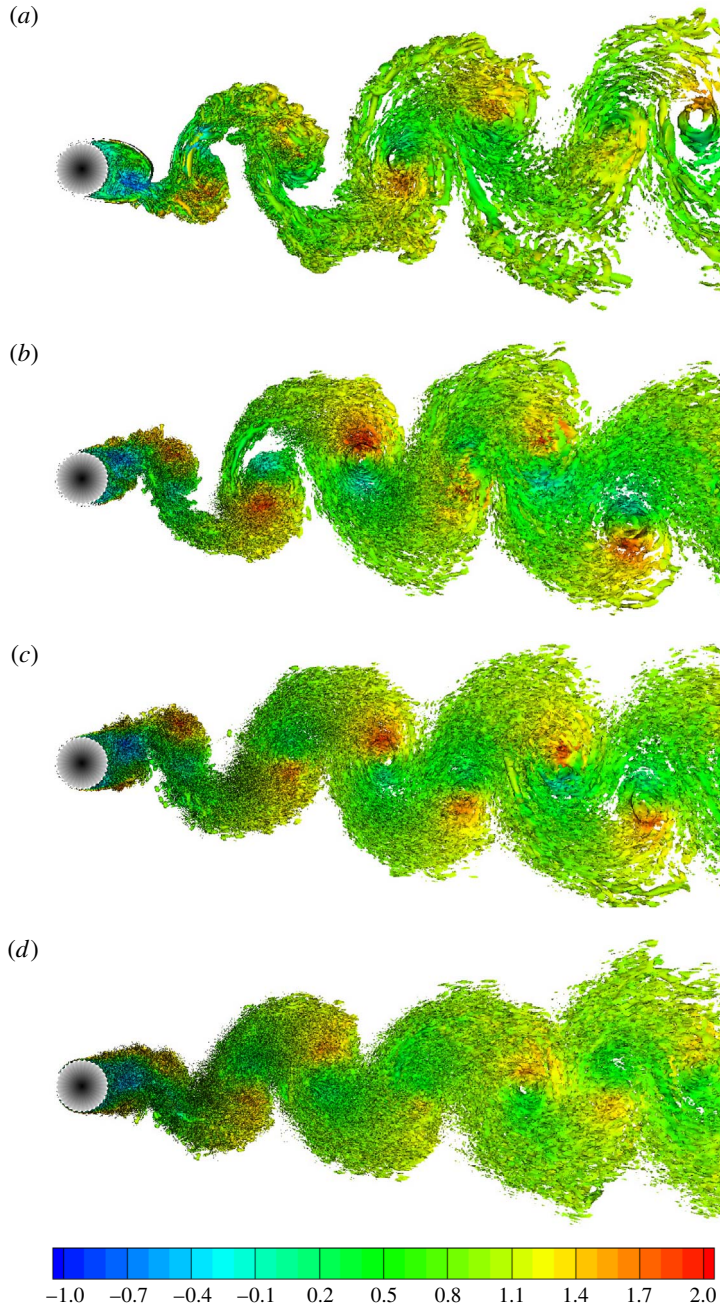
(*a*)

(*b*)

(*c*)

(*d*)

$$-1.0 \quad -0.7 \quad -0.4 \quad -0.1 \quad 0.2 \quad 0.5 \quad 0.8 \quad 1.1 \quad 1.4 \quad 1.7 \quad 2.0$$

FIGURE 23. Instantaneous wake flow. $Q = 1$ and coloured by u_x. (*a*) $Re_D = 3.9 \times 10^3$; (*b*) $Re_D = 1 \times 10^4$; (*c*) $Re_D = 2 \times 10^4$; (*d*) $Re_D = 5 \times 10^4$.

flow, we can consider the structure and location of the secondary/prior separation bubble as a signature of transition between regimes. In the subcritical regime, a secondary separation bubble exists inside the primary mean-flow recirculation bubble. During transition to the supercritical regime, the mean-flow secondary separation
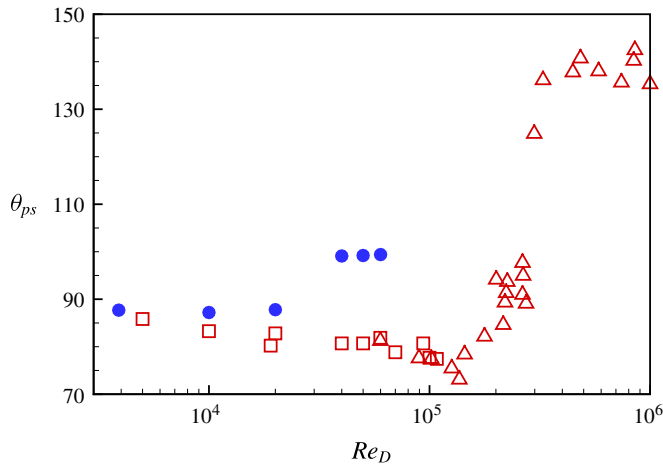
FIGURE 24. (Colour online) Separation angle of the primary separation θ_{ps}: $\square$, experiment by Son & Hanratty (1969); $\triangle$, experiment by Achenbach (1968); $\bullet$, present LES, $\epsilon/D = 1/32$ and $k = 32$.

bubble disappears followed, as Re_D increases, by the creation of a prior separation bubble initially just upstream of the primary separation line. At higher Re_D, as the flow transitions to a transcritical state, the prior separation bubble itself vanishes and only primary mean-flow separation exists within the whole flow field (Cheng *et al.* 2017). For subcritical flow, turbulent transition lies inside the wake flow and moves onto the highly sheared subregion that lies between the primary mean-flow separation line and the reattaching secondary bubble. For supercritical flows, the local Reynolds number is sufficiently large that transition to turbulence takes place on the upper surface of the (now) prior separation bubble while for transcritical flow, turbulent transition takes place directly within the boundary layer on the surface of the cylinder. For the subcritical regime with $Re_D > 10^4$, C_D is nearly constant at approximately $C_D = 1.25$. After a sudden drop, the drag coefficient decreases to approximately $C_D = 0.3$ and remains at this value for a large range of Re_D. This is recognized as the supercritical regime. In the transcritical regime, C_D grows again and reaches a nearly constant value $C_D \approx 0.7$ (Roshko 1961).

The total drag around cylinder is the sum of the pressure drag (or form drag) and skin-friction drag. The form drag is mainly controlled by the position of the mean-flow primary separation angle θ_{ps}. In general, larger values of θ_{ps} indicate a smaller leeward region of base pressure and therefore smaller total drag. Within the supercritical regime in the smooth-cylinder flow, laminar–turbulent transition takes place on a prior separation bubble. The reattached turbulent flow results in an energized turbulent boundary layer that can resist an adverse pressure gradient more effectively than a laminar boundary layer. This in turn delays mean-flow separation with the result that the primary mean-flow separation point can be up to $\theta_{ps} = 140°$, corresponding to a low drag coefficient $C_D \approx 0.3$. Experimental measurements of θ_{ps} versus Re_D (Son & Hanratty 1969) for the smooth-wall cylinder flow are shown in figure 24 where the rapid increase through the drag crisis is clearly evident.

Also shown in figure 24 are values of (θ_{ps}, Re_D) for our LES of the grooved-cylinder flow with fixed $\epsilon/D = 1/32$. These show a much smaller change through the drag crisis and into the beginning of the transcritical regime in comparison with the
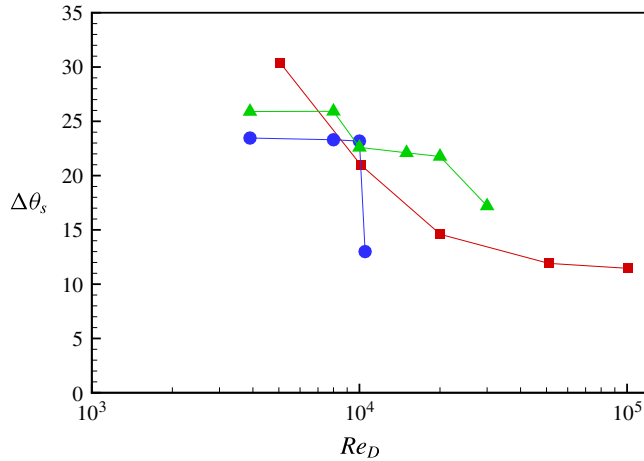
FIGURE 25. (Colour online) Angle between the primary separation point and the reattachment point of the secondary separation bubble $\Delta\theta_s$: ■, LES for smooth cylinder (Cheng *et al.* 2017); ●, present LES, $\epsilon/D = 1/32$ and $k = 32$; ▲, present LES $\epsilon/D = 1/32$ and $k = 64$.

smooth-wall flow. Although the present LES penetrates only the lower Re_D range of the transcritical regime for the grooved-cylinder flow, figure 3 of Achenbach & Heinecke (1981) indicates that for several rough-surface cylinder flows C_D, and hence also θ_{ps}, remains sensibly constant far into the transcritical regime. This suggests that, for the non-smooth surface case, especially for large grooves or three-dimensional periodic surface shapes, laminar–turbulent flow transition is not the underlying mechanism that stimulates the drag crisis at much lower Re_D than for the smooth-wall flow. Instead, while for the present grooved-cylinder flow, prior separation bubbles still exist into the supercritical regime, these can be trapped in cavities formed by the specific groove geometry of the cylinder surface. Unlike the smooth-wall cylinder flow, these bubbles do not appear to be associated with turbulent boundary-layer transition. The drag crisis is then essentially a laminar flow phenomenon. Like the smooth-wall case, the drag crisis is still stimulated by an equivalent secondary separation bubble moving to smaller θ as Re_D is increased, interacting with the primary near-wall separation flow and then passing upstream of θ_{ps} and undergoing a change into a prior separation bubble. But turbulent boundary-layer transition plays no dynamical role. The drag crisis, with a small increase in θ_{ps} is simply a dynamical response of the overall flow to the shrinking and upstream migration behaviour of the secondary separation bubble while the near-wall flow remains laminar.

   Hence, for a specific geometry, the primary mean-flow separation line does not reach large θ_{ps} in the supercritical regime. The result is that, following the drag crisis in both the supercritical and transcritical flow regimes, C_D reaches minimum and constant values respectively that are rather larger than for the smooth-walled cylinder flow. For example, in the present LES with $k = 32$ and $\epsilon/D = 1/32$, the minimal drag coefficient is about 0.7, which is similar to the strongest roughness case in experiment by Achenbach & Heinecke (1981) and substantially larger than $C_D|_{min} \approx 0.3$ for the smooth-cylinder flow.
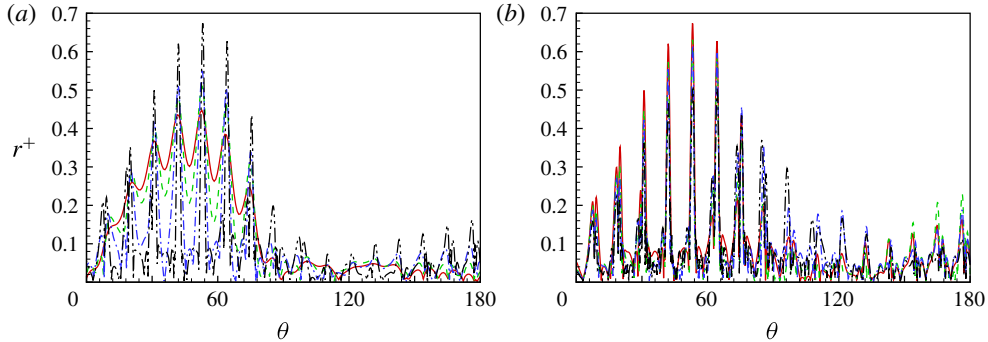
FIGURE 26. (Colour online) Plots of r^+. (a) Cases with $Re_D = 3900$ and varying ϵ/D: ——, 1/320; – – – –, 1/160; — · —, 1/80; — · · —, 1/32. (b) Cases with $\epsilon = 1/32$ and varying Re_D: ——, 3900; – – – –, 10^4; — · —, 2×10^4; — · · —, 5×10^4.
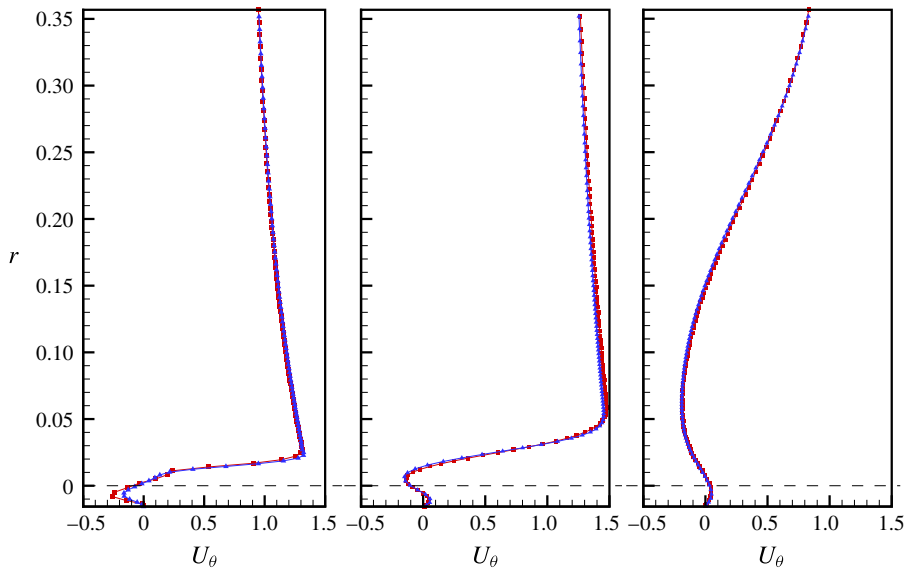

FIGURE 27. (Colour online) Comparison of velocity U_θ for case $k = 32$, $\epsilon/D = 1/32$ and $Re_D = 2 \times 10^4$: ■, fine mesh; ▼, coarse mesh.

6.2. *Angle between primary separation bubble and secondary separation bubble*

Transition from the subcritical to the supercritical flow regimes, which is typically named the drag crisis, is clearly related to separation flow behaviour around the cylinder. A useful diagnostic, implemented both experimentally (Son & Hanratty 1969) and numerically (Cheng *et al.* 2017) for smooth-cylinder flow, is the angle between the separation point of the primary separation bubble and the reattachment point of the secondary separation bubble, here defined as $\Delta\theta_s$. LES data for $\Delta\theta_s$ are shown in figure 25 where the symbol ■ denotes LES results for the smooth-cylinder case (Cheng *et al.* 2017). It can be seen that in smooth-wall cylinder flow, $\Delta\theta_s$ decreases monotonically from 30° at $Re_D = 5000$ to around 10° at $Re_D = 10^5$. It is notable that the slope of $\Delta\theta_s$ with increasing Re_D decreases at $Re_D = 10^5$. In fact we do not expect that $\Delta\theta_s$ can reach $\Delta\theta_s = 0$ at the onset of the drag crisis as the flow

transitions into the supercritical regime. A plausible explanation is that, when $\Delta\theta_s$ decreases to about 10°, a strong shear layer forms defined/bounded by the primary separation zone and the reattaching secondary separation flow. The instantaneous realizations of this local flow structure are strongly three-dimensional as shown in the instantaneous skin-friction plots of Cheng *et al.* (2017). Such shear layers are expected to be strongly Kelvin–Helmholtz unstable at Re_D near the drag crisis (for both smooth- and rough-walled flows) and it can be expected that this may well inhibit the formation of a coherent mean-flow secondary separation bubble as the overall flow moves into the drag crisis. This suggests that $\Delta\theta_s = O(10°)$ can be considered as an approximate asymptotic value for $\Delta\theta_s$ in the subcritical regime for smooth-cylinder flow.

In figure 25, data with the symbol ● are from the present LES with $k = 32$ and $\epsilon/D = 1/32$. Since the separation bubble can only be bounded by the physical wall, $\Delta\theta_s(Re_D)$ in the grooved-cylinder flow cannot show a continuously changing variation. Instead, $\Delta\theta_s$ remains constant at around $\Delta\theta_s = 23°$, and then jumps to around $\Delta\theta_s = 12°$ when approaching the transition to supercritical flow. This jump corresponds to the flow field change in figure 15, from figure 15(*c*) to figure 15(*d*). For the geometry with $k = 32$, each groove spans approximately 11°, which is comparable to the sudden decrease in $\Delta\theta_s$ for the grooved-cylinder flow as the drag crisis is approached. This suggests a mean-flow secondary separation reattachment line that tends to occur on groove crests.

To provide further data, we implemented a further set of LES, with $k = 64$, $\epsilon/D = 1/32$ and varying Re_D from 3900 to 3×10^4. $\Delta\theta_s$ for these LES are shown in figure 25, labelled with the symbol ▼. The parameters of these LES are summarized in table 5. In these cases, each groove covers about 5.6°. The behaviour of $\Delta\theta_s(Re_D)$ is similar to both the smooth- and groove-walled cylinder flows with $k = 32$. Starting from $Re_D = 3.9 \times 10^3$, $\Delta\theta_s \approx 26°$, $\Delta\theta_s$ then jumps to approximately 22° at approximately $Re_D = 10^4$. Further increasing Re_D to 3×10^4 shows a further jump to 17°. For these LES, although transition to the supercritical regime has not been reached at the maximum Re_D, $\Delta\theta_s$ clearly shows a decreasing tendency similar to the movement of the mean-flow secondary separation bubble for our other LES.

7. Concluding remarks

Wall-resolved LES has been used to study flow over a spanwise grooved cylinder. Results from two main sets of LES have been described, the first on different amplitude grooves at fixed $Re_D = 3.9 \times 10^3$, and the second set with fixed groove geometry but with varying Re_D from 3.9×10^3 to 6×10^4 to cover different flow regimes.

For flows with fixed $Re_D = 3.9 \times 10^3$, we focused on flow deviations from the smooth-cylinder case at the same Re_D. It is generally found that increasing the groove magnitude ϵ/D will result in flow changes which in some respects are similar to those observed in increasing Re_D for smooth-cylinder flows. These include the shrinking of the recirculation bubble and the maintenance of a near-constant minimal pressure coefficient. Some flow characteristics for the grooved cylinder are found to be rather different from the smooth-cylinder case, especially the azimuthal variation of the azimuthal skin-friction coefficient. For grooves with larger ϵ/D, there are locally trapped separation bubbles formed as cavity flows within each groove. Also of interest is the surface distribution of the non-dimensional pressure gradient parameter β, which is a function of boundary-layer thickness, wall shear stress and pressure

gradient. This parameter is found to be nearly constant on the windward part of the cylinder for the smooth-cylinder case but shows strong oscillatory azimuthal variation for the grooved-cylinder flow.

For geometries with large amplitude grooves, we extend LES up to $Re_D \sim 6 \times 10^4$, which reaches the beginning of the transcritical regime. For subcritical regime flows with Re_D up to 10^4, a secondary separation bubble is clearly observed. As Re_D is increased this bubble moves upstream and reduces in size. For supercritical flows, a complex near-wall flow pattern comprising the coexistence of clockwise and anti-clockwise flowing mean-flow cavity-like bubbles are observed in grooves upstream of the primary separation bubble. This anti-clockwise bubble can be identified as the grooved-cylinder flow equivalent of a prior separation bubble for flow over smooth cylinder.

The comparison of near-wall flow behaviour at the drag crisis for the smooth-wall LES of Cheng *et al.* (2017) and the present LES of flow past a grooved-wall cylinder at ϵ/D is perhaps informative. The smooth-wall case is clearly an example of a drag crisis for a flow that can be thought of as wall-bounded in the sense that it contains a developing boundary layer that exhibits laminar–turbulent transition at or near the onset of the drag crisis. In contrast the grooved-wall cylinder flow is not a canonical wall-bounded flow because there exists no recognizable, coherent boundary layer. Rather, the near-wall local flow resembles relatively low Reynolds number flow over obstacles/cavities – the grooves – producing mean-flow trapped separation bubbles and a complex three-dimensional instantaneous skin-friction field.

Yet the two flows share one striking common feature which is the presence of a mean-flow, secondary separation bubble that diminishes and subsequently vanishes, transforming into upstream local flow features, as the flows pass through their respective drag crises. This suggests that the primary mechanism for production of the drag crisis, at least for cylinder flows, is not in fact associated with laminar–turbulent boundary-layer transition. We hypothesize that the generic drag crisis mechanism in fact originates via the interaction of recirculating back flow motions, visible in the mean as a reattaching, mean-flow secondary separation bubble, with the local near-wall primary separation flow. The details perhaps involve proximity to the cylinder wall of incipient shear layer, Kelvin–Helmholtz-like instability triggering a global change in flow state that produces a sudden streamwise shift of the mean-flow separation line, a subsequent change in base pressure and a corresponding reduction in drag. In this scenario, for the smooth-wall case, boundary-layer transition is probably stimulated by and substantially enhances the global flow change, but is not its primary cause.

For the grooved-cylinder flow, at least for moderate sized grooves, this suggests that the drag crisis is then an almost entirely laminar phenomenon. The existence of a quantifiable mechanism for this interpretation of the drag crisis remains an open question (which we do not claim to answer), as does the question of whether this interpretation is valid for general cylinder flows with surface perturbations different from those studied presently, and that may include, for example the strongest R3DP case documented in Achenbach & Heinecke (1981), and also traditional small-scale, surface roughness internal to the local boundary layer. These questions await further exploration.

Acknowledgements

Appendix A. Mesh verification

Wall-resolved large-eddy simulation should fully resolve the near-wall flow. It is generally considered that minimally, 5–7 mesh points normal to the wall are required for resolving the viscous sublayer. A typical parameter in wall-resolved LES is the ratio of the near-wall, wall-normal mesh size Δr to the viscous length scale $l^+ = u_\tau/\nu$. For the present cell-centred mesh arrangement with $r^+ = \Delta r/l^+$, the requirement is generally that $r^+ < 1$ ideally (Choi & Moin 2012). In LES by Cheng *et al.* (2017), cases and regions with $r^+ < 1$ show results for $C_{f\theta}$ using direct wall-normal differentiation of the wall-parallel velocity to be in good agreement with experiment, while those with $r^+ > 1$ show a relatively large difference from both experimental measurements and other methods of determining $C_{f\theta}$. In figure 26, we show r^+ for cases in the two sets of LES reported presently. Since the present LES still has $Re_D \sim 5 \times 10^4$ or lower, $r^+ < 1$ can be seen to be reasonably satisfied.

For verification, we implemented two meshes for the case with $Re_D = 2 \times 10^4$, $k = 32$ and $\epsilon/D = 1/32$. The mesh in the wall-normal direction is fixed while different mesh sizes for the circumferential and spanwise directions are used. The mesh $N_\theta \times N_y \times N_r$ is $2048 \times 128 \times 512$ for the fine grid and $1024 \times 64 \times 512$ for the coarse grid. To show convergence, in figure 27 we plot the wall-parallel velocities at three different locations, which are at the trough of three grooves, one windward at around $x = -0.15$, one around the peak of the cylinder and one leeward at about $x = 0.2$. It is generally found that the velocity profiles agree well for results using the two meshes. The verification case is at $Re_D = 2 \times 10^4$. This provides evidence that the present mesh is sufficiently fine for the present study.

Appendix B. Thwaites' method for smooth cylinder

In analysing laminar boundary-layer flow, Thwaites (1949) found a uni-parametric correlation formula

$$2T - 2(H+2)\lambda = 0.45 - 6.0\lambda, \tag{B 1}$$

with

$$H = \frac{\delta^*}{\hat{\theta}} \quad T = \frac{\tau_w \hat{\theta}}{\nu U_e} \quad \lambda = U_e' \frac{\hat{\theta}^2}{\nu}. \tag{B 2a-c}$$

Here $\hat{\theta}$ is the momentum boundary-layer thickness. U_e is the external velocity in the wall-parallel direction and the superscript prime ' $'$ ' denotes its derivative along the θ direction. With this collapse formula, the momentum integration equation can be reduced to

$$\frac{\hat{\theta}^2(\theta)}{\nu} = \frac{\hat{\theta}_0^2}{\nu} \left(\frac{U_e^0}{U_e(\theta)} \right)^6 + \frac{0.45}{U_e} \int_0^\theta \left(\frac{U_e(\phi)}{U_e(\theta)} \right)^5 \, d\phi. \tag{B 3}$$

The integration of the above equation can be done analytically when an outer velocity profile U_e is known. For flow over a smooth circular cylinder, according to LES by Cheng *et al.* (2017), $U_e \approx 1.5 \sin(1.25\theta)$ for subcritical cases and $U_e \approx 2 \sin\theta$ (potential flow) for supercritical cases. Using this U_e, (B 3) can be solved to give

$$\lambda = 0.075 \left(1 - \tfrac{7}{2}\sin^2(\theta/2) + \tfrac{18}{5}\sin^4(\theta/2) - \tfrac{6}{5}\sin^6(\theta/2) \right) (1 - \sin^2(\theta/2))^{-3}, \tag{B 4}$$

for supercritical cases (Sherman 1990). With λ known, β can be derived as

$$\beta = \frac{H\lambda}{T} \frac{1}{U_e' U_e} \frac{\partial p}{\partial \theta}. \tag{B 5}$$

Plotting (B 4) (not shown) indicates that $\lambda \approx 0.075$ for a large range of θ. Then β can be calculated as $\beta \approx -0.502$ for a similar θ range. The above estimate excludes $\theta = 0$. Here the local solution for stagnation point (Hiemenz) flow should be used to estimate θ (not shown here). For further details concerning Thwaites' method for the smooth cylinder, see Sherman (1990).

REFERENCES

ACHENBACH, E. 1968 Distribuion of local pressure and skin friction around a circular cylinder in cross-flow up to $Re = 5 \times 10^6$. *J. Fluid Mech.* **34**, 625–639.

ACHENBACH, E. 1971 Influence of surface roughness on the cross-flow around a circular cylinder. *J. Fluid Mech.* **46**, 321–335.

ACHENBACH, E. & HEINECKE, E. 1981 On vortex shedding from smooth and rough cylinders in the range of Reynolds numbers 6×10^3 to 5×10^6. *J. Fluid Mech.* **109**, 239–251.

BEAUDAN, P. & MOIN, P. 1994 Numerical experiments on the flow past a circular cylinder at sub-critical Reynolds number. *Tech. Rep.* TF-62. Stanford University.

BREUER, M. 2000 A challenging test case for large eddy simulation: high Reynolds number circular cylinder flow. *Intl J. Heat Fluid Flow* **21**, 648–654.

CARDELL, G. S. 1993 Flow past a circular cylinder with a permeable splitter plate. PhD thesis, California Institute of Technology.

CHAKRABORTY, P., BALACHANDAR, S. & ADRIAN, R. J. 2005 On the relationships between local vortex identification schemes. *J. Fluid Mech.* **535**, 189–214.

CHENG, W., PULLIN, D. I. & SAMTANEY, R. 2015 Large-eddy simulation of separation and reattachment of a flat plate turbulent boundary layer. *J. Fluid Mech.* **785**, 78–108.

CHENG, W., PULLIN, D. I., SAMTANEY, R., ZHANG, W. & GAO, W. 2017 Large-eddy simulation of flow over a cylinder with Re_D from 3.9×10^3 to 8.5×10^5: a skin-friction perspective. *J. Fluid Mech.* **820**, 121–158.

CHOI, H. & MOIN, P. 2012 Grid-point requirements for large eddy simulation: Chapman's estimates revisited. *Phys. Fluids* **24**, 011702.

CHUNG, D. & PULLIN, D. I. 2009 Large-eddy simulation and wall modelling of turbulent channel flow. *J. Fluid Mech.* **631**, 281–309.

FAGE, A. & WARSAP, J. H. 1929 The effects of turbulence and surface roughness on the drag of a circular cylinder. *Tech. Rep.* 1283. Reports and Memoranda.

GÜVEN, O., FARELL, C. & PATEL, V. C. 1980 Surface-roughness effects on the mean flow past circular cylinders. *J. Fluid Mech.* **98**, 673–701.

JIMÉNEZ, J. 2004 Turbulent flows over rough walls. *Annu. Rev. Fluid Mech.* **36**, 173–196.

KARNIADAKIS, G. E. & TRIANTAFYLLOU, G. S. 1992 Three-dimensional dynamics and transition to turbulence in the wake of bluff objects. *J. Fluid Mech.* **238**, 1–30.

KRAVCHENKO, A. G. & MOIN, P. 2000 Numerical studies of flow over a circular cylinder at $Re_D = 3900$. *Phys. Fluids* **12**, 403–417.

LEHMKUHL, O., RODRIGUEZ, I., BORRELL, R., CHIVA, J. & OLIVA, A. 2014 Unsteady forces on a circular cylinder at critical Reynolds numbers. *Phys. Fluids* **26**, 4904415.

MISRA, A. & PULLIN, D. I. 1997 A vortex-based subgrid stress model for large-eddy simulation. *Phys. Fluids* **9**, 2443–2454.

MITTAL, R. & BALACHANDAR, S. 1996 Direct numerical simulation of flow past elliptic cylinders. *J. Comput. Phys.* **124**, 351–367.

ROSHKO, A. 1961 Experiments on the flow past a circular cylinder at very high Reynolds number. *J. Fluid Mech.* **10**, 345–356.

SAYADI, T., HAMMAN, C. W. & MOIN, P. 2013 Direct numerical simulation of complete H-type and K-type transitions with implications for the dynamics of turbulent boundary layers. *J. Fluid Mech.* **724**, 480–509.

SCHEWE, G. 1983 On the force fluctuations acting on a circular cylinder in crossflow from subcritical up to transcritical Reynolds numbers. *J. Fluid Mech.* **133**, 265–285.

SHERMAN, F. S. 1990 *Viscous Flow*. McGraw-Hill.

SON, J. S. & HANRATTY, T. J. 1969 Velocity gradients at the wall for flow around a cylinder at Reynolds numbers from 5×10^3 to 10^5. *J. Fluid Mech.* **35**, 353–368.

SPALART, P. R., MOSER, R. D. & ROGERS, M. M. 1991 Spectral methods for the Navier–Stokes equations with one finite and two periodic directions. *J. Comput. Phys.* **96**, 297–324.

SZECHENYI, E. 1975 Supercritical Reynolds number simulation for two-dimensional flow over circular cylinders. *J. Fluid Mech.* **70**, 529–542.

THWAITES, B. 1949 Approximate calculation of the laminar boundary layer. *Aeronaut. Q.* **1**, 245–280.

VOELKL, T., PULLIN, D. I. & CHAN, D. C. 2000 A physical-space version of the stretched-vortex subgrid-stress model for large-eddy simulation. *Phys. Fluids* **228**, 2426–2442.

WEIDMAN, P. 1968 Wake transition and blockage effects on cylinder base pressures. PhD thesis, California Institute of Technology.

YAMAGISHI, Y. & OKI, M. 2004 Effect of groove shape on flow characteristics around a circular cylinder with grooves. *J. Vis.* **7**, 209–216.

ZANG, Y., STREET, R. L. & KOSEFF, J. R. 1994 A non-staggered grid, fractional step method for time-dependent incompressible Navier–Stokes equations in curvilinear coordinates. *J. Comput. Phys.* **114**, 18–33.

ZHANG, W., CHENG, W., GAO, W., QAMAR, A. & SAMTANEY, R. 2015 Geometrical effects on the airfoil flow separation and transition. *Comput. Fluids* **15**, 60–73.